University of Žilina
Faculty of Management Science and Informatics

Computational analysis of inertial effects in microchannels

Dissertation Thesis

Registration number: 2836002023006

Study program:	Applied Informatics
Field of study:	Informatics
Affiliation:	Faculty of Management Science and Informatics,
	Department of Software Technologies,
	University of Žilina
Supervisor:	prof. Mgr. Ivan Cimrák, Dr.

Žilina, 2023   Mgr. Alžbeta Bugáňová

Annotation

Type of the work:	Dissertation
Academic year:	2022/2023
Title of the work:	Computational analysis of inertial effects in microchannels
Author:	Mgr. Alžbeta Bugáňová
Supervisor:	prof. Mgr. Ivan Cimrák, Dr.
Supervisor specialist:	Mgr. Kristína Ďuračíková Kovalčíková, PhD.
Language:	English
Number of pages:	111
Number of figures:	50
Number of tables:	7
Number of references:	39
Keywords:	Dean number, Reynolds number, inertial microfluidics, rectangular cross-section, particle separation, focusing length

Acknowledgments

Thank you. I want to sincerely thank the people who have been with me during my doctoral studies.

First of all, I thank prof. Ivan Cimrák, my supervisor, for professional guidance and advice, for always kindly provided information about the performance of his code, for listening to my complaints and excuses and for the nudges necessary to get me all the way to this point. Thank you for all the supervising.

I thank Mgr. Kristína Ďuračíková Kovalčíková, PhD., my supervisor specialist, for being available anytime. Thank you for all the advice and help before conferences, without which I would be lost sometimes.

I thank Michal Mulík, Adam Mračko, Dominika Petríková, Betka Bohiníková, Iveta Jančigová - my colleagues in the cell-in-fluid research group for both the on-topic and off-topic stimulating discussions. Especially, thank you, Michal and Adam, for the willingness to always answer my questions in python and for code-related support.

Finally, I want to thank my family, my husband Michal, my mum Dana, my grandparents Katarína and Stanislav, for their support in ensuring that I had the best conditions possible for my work and for a chance to attend international conferences. I want also thank my children Adam and Nene for their hugs and smile which I often really needed.

Statutory declaration

I declare that I have written the submitted dissertation independently. I did not use any outside support except for the quoted literature and other sources mentioned in the dissertation.

In Žilina, 12. April 2023   Mgr. Alžbeta Bugáňová

Abstract

Alžbeta Bugáňová: Computational analysis of inertial effects in microchannels (Dissertation thesis) – The University of Žilina, Faculty of Management Science and Informatics, Department of Software Technologies – Supervisor: prof. Mgr. Ivan Cimrák, Dr. – Supervisor specialist: Mgr. Kristína Ďuračíková Kovalčíková, PhD. – Qualification level: Doctor of Philosophy in Applied Informatics – EDIS Žilina, April 2023 - 111 pages.

The dissertation thesis deals with inertial flows in curved channels. In the first part, we describe the long process of setting up a suitable geometry for simulations and approximations of continuous periodic flow based on particle reseeding immersed to the flow. We also analyze a suitable method for moving the fluid in the simulation box. Next, we observe the Dean effect in the torus, in the cylindrical ring with square cross-section, and in the helix. We compare the results of simulations with different settings of fluid velocity, channel curvature, kinematic viscosity and pitch in the case of a helix. In the second part of the work, we analyze a serpentine curved channel with a rectangular cross-section with different settings of channel height and width and particle size at four different Reynolds numbers. We describe the particle focusing and the focusing length, which is necessary for the separation of the particles, which was the main goal of the work. In the last part, we propose and analyze the roughness elements in curved channel. A public available computational model was used as part of the open source scientific computing package ESPResSo. The results should serve for further analysis of suitable channel geometries for particle separation performance.

Keywords: Dean number, Reynolds number, inertial microfluidics, rectangular cross-section, particle separation, particle seeding, focusing length

Abstrakt

ALŽBETA BUGÁŇOVÁ: Výpočtová analýza inerciálnych efektov v mikrokanáloch (dizertačná práca) – Žilinská univerzita v Žiline, Fakulta riadenia a informatiky, Katedra softvérových technológií – Školiteľ: prof. Mgr. Ivan Cimrák, Dr. – Školiteľ špecialista: Mgr. Kristína Ďuračíková Kovalčíková, PhD. – Stupeň odbornej kvalifikácie: philosophiae doctor v odbore Aplikovaná informatika - EDIS Žilina, apríl 2023 - 111 strán.

Dizertačná práca sa zaoberá inerciálnymi tokmi v zahnutých kanáloch. V prvej časti opisujeme dlhý proces nastavenia vhodnej geometrie pre simulácie a aproximácie neprerušeného periodického toku na základe premiestňovania častíc vnorených do toku. Analyzujeme tiež vhodnú metódu na rozpohybovanie tekutiny v simulačnom boxe. Ďalej sledujeme Deanov efekt v toruse, vo valci so štvorcovým prierezom a v špirále. Porovnávame výsledky simulácií pri rôznych nastaveniach rýchlosti tekutiny, zahnutia kanálu, kinematickej viskozity a závitu v prípade helixy. V druhej časti práce analyzujeme zahnutý kanál s obdĺžnikovým prierezom s rôznymi nastaveniami výšky a šírky kanála a veľkosti častíc pri štyroch rôznych Reynoldsových číslach. Popisujeme umiestňovanie častíc a dĺžku procesu ich zaostrovania, ktorá je potrebná na separáciu častíc, čo bolo hlavným cieľom práce. V poslednej časti navrhujeme a analyzujeme zdrsnenie zakriveného kanála. Využitý bol verejne dostupný výpočtový model ako súčasť open source vedeckého výpočtového balíka ESPResSo. Výsledky by mali slúžiť na ďalšiu analýzu vhodných geometrií kanálov pre triedenie buniek.

Kľúčové slová: Deanove číslo, Reynoldsove číslo, inercálne mikrokanály, obdĺžnikový prierez, separácia častíc, rozmiestňovanie častíc, dĺžka zaostrovania

Contents

14

List of Figures

15

List of Tables

List of Abbreviations

CEA	**C**ontraction **E**xpansion **A**rray
Cif-BMCG	**C**ell **i**n **f**luid - **B**iomedical **M**odeling and **C**omputations **G**roup
CTC	**C**irculating **T**umor **C**ell
ESPResSo	**E**xtensible **S**imulation **P**ackage for **Res**earch on **So**ft matter systems
MIT	**M**assachusetts **I**nstitute of **T**echnology
PyOIF	**P**ython **O**bject - **I**n - **F**luid
RBC	**R**ed **B**lood **C**ell
WBC	**W**hite **B**lood **C**ell

1 Introduction

Modeling of biological experiments is a relatively large field that has received a lot of attention in recent years. There are a number of different approaches for modeling. The questions that the model is supposed to answer affect the level of detail in which computer simulations need to be created. One of the many goals of research in biomedicine is to investigate the behavior of cancer cells. Laboratory experiments that deal with this issue use the so-called microfluidic devices where they monitor the movement of cells. However, it is very technologically, financially and time-consuming to create new and new prototypes. Computational models simulating processes in such devices in many cases of prototype production they can replace. With the help of numerical simulations, we can model cell flows in microfluidic devices, which we then analyze and evaluate under different conditions and with different parameter settings.

Circulating tumor cells (CTCs) are the main reason for cancer metastizing. The initial worldwide motivation is design and optimization of microfluidic devices able to separate CTCs from the rest of other blood cells in blood samples of patients in the future. The design is still under research, but the computer simulations significantly improve the design process because they save both - huge costs and also the development. Therefore, there is a must for a model of blood flow and particles immersed in a channel with many types of obstacles.

At the University of Žilina, the research group Cell-in-fluid Biomedical Modeling and Computations Group [4], from here referred to as Cif-BMCG, is dedicated to these models, which creates and improves computational models and their implementation, based on two components: liquid and elastic objects embedded in it. The liquid represents blood plasma, or another liquid, and the elastic objects represent red blood cells, white blood cells, and other cells (for example, cancer cells). Thanks to the discretization of their surface, the cells can deform and also interact with the

liquid. The dissertation thesis deals with the Dean effect and its analysis. We tried to simulate devices for the purpose of separating objects found in the blood. The biomedical motivation for the given topic is written in its introduction, 1.1. In individual chapters, we tried to illustrate the results with illustrative examples using pictures and graphs. At the end, the achieved partial results are summarized as well as a proposal for further steps for the following research. The work is complemented by a list of published articles and literature that motivated us to the given topic and from which we drew the theoretical basis.

I consider the topic to be very actual because the use of computer simulations in the field of designing the parameters of microfluidic devices is one of the problems that several research centers around the world are currently working on.

1.1 Biomedical motivation

At the beginning, there was a motivation based on the article about a special spiral microchannel with Dean's effect use. It could be kind of help for people with cancer. In Figure 1.1 is an example of this special spiral microchannel with trapezoidal cross-section, where we can see an impact of Dean's effect and its ability in praxis. The Dean effect in this channel causes cells of different sizes to mix. When we imagine the beginning of a channel with a fluid flow, into which we put a sample with larger-cancer cells and smaller cells normally found in human blood (red blood cells (RBCs), white blood cells (WBCs), platelets, ...), the individual particles start to mix randomly inside the flow. After some time in the flow, we can observe the smaller components will start to accumulate near the outer wall of the channel, while the larger cells will accumulate on the inner wall of the channel [35]. It means, blood particles are focusing to two places based on their size. Consequently, at some step we could separate the cancer cells and the other hematological components into an outer and an inner duct and collect them in two different containers [35]. Thanks to this, we would be able to separate cancer cells from others.
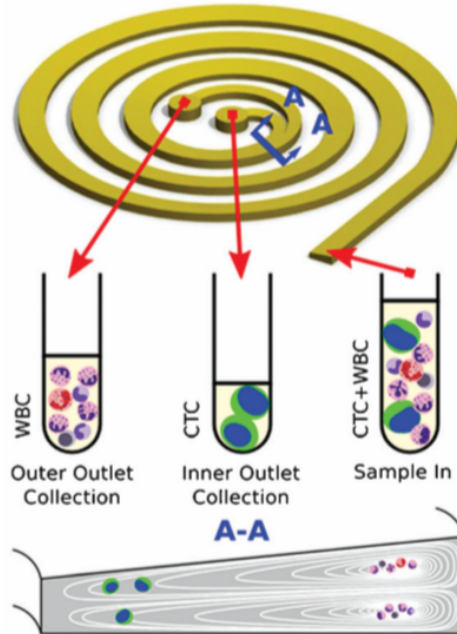
Figure 1.1: Spiral microchannel with trapezoidal cross-section. Reprented from [35].

1.2 Aims of present work

Computational modelling can be a strong tool in the design of microfluidic channels. The key assumption however is the setting of appropriate parameters of the model so that the computational model represents the reality.

The very general idea behind the research within this thesis was to look at the separating of particles of different sizes. There are numerous methods and we chose inertial microfluidics because of their ability to separate particles or cells in a gentle way - no large deformations for the cells, no necessity to squeeze between the pores in a filter, no activation of cells with antibodies.

While there are several research groups around the world modeling blood flow in microfluidic devices, there are also several types of channels used in inertial microfluidics. According to the shape of the channel, we can divided inertial microfluidics to straight, spiral, serpentine channels, contraction-expansion array (CEA) and zig-zag channels. All of them have common feature - the ability to branch the main channel at the end into more output channels collecting particles of different sizes or a particle-free fluid, see Figure 1.2. So the important part of the thesis is to determine which geometry to use.
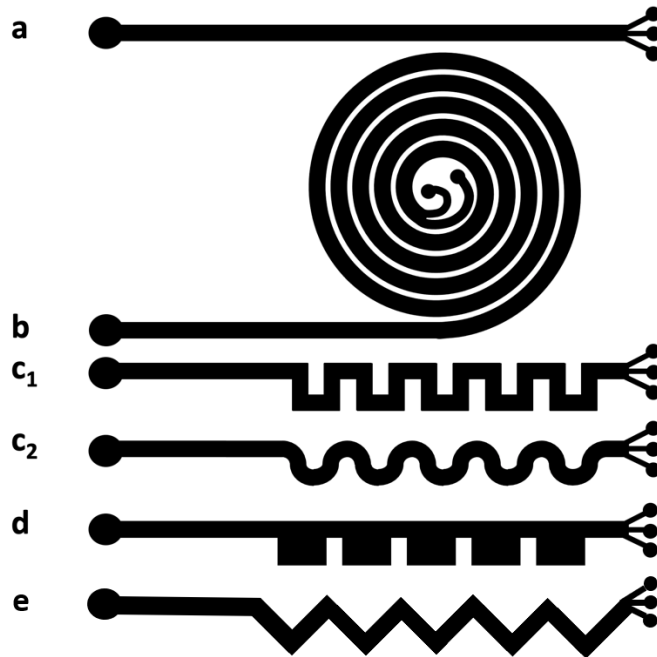
Figure 1.2: Typical shapes of channels used in inertial microfluidics (a) straight (b) spiral (c_1) square serpentine (c_2) curved serpentine (d) CEA and (e) zig-zag channels. Large black circles represent inflow of the suspension and several smaller circles represent outflow with separated particles.

The main objective of the thesis is to get better understanding of inertial effects in flow of particles and cells inside curvilinear microfluidic channels with focus on a concrete channel geometry.

Partial objectives leading to this goal:

- **Analysis of Dean flow in different channel geometries and determination of a concrete channel geometry.**

  First of all, we need to study existing research about particle separation in microfluidic devices. After literature comparison, we need to design a suitable channel geometry for Dean effect verification and also a suitable channel geometry for particle separation using ESSPResSo and PyOif package. We need to compare various parameter settings in several cross-sections of curved channel. We will analyze average fluid velocity, curvature radius, section radius, pitch and kinematic viscosity. Our aim is to find out whether the position of the fastest flow in channel cross-section is affected only by parameters from

Dean's number formula. We need to know the most suitable channel geometry so that the computational model is capable of correctly modelling the inertial effects.

- **Determining the stable positions of particles in a curved channel.**

Using the proposed designed microchannels, we will analyze the effect of particle immersed in simulations. We need to determine the stable positions of particles in curved channels.

- **Channel geometry optimization for optimal separation**

For the purpose of the best particle separation performance, we will create a new channel geometry with three different squared cross-sections. A proposal of microchannel parameters, which will allow to separate two types of particles, differing in their size, will be analysed.

1.3 Thesis outline

After introduction, biomedical motivation and aims of the work at the beginning, in Chapter 2, we describe current state-of-the-art based on experimental studies where the inertial effects in microchannels and numerical simulations are discussed. Then you can find an outline of the physical properties of fluid model, sphere particles and their behavior in flow. We specifically point out those specific characteristics that are considered most important in modelling of blood flow in microfluidic devices and their focusing and separating. We mentioned there information technology and software used for simulations.

In Chapter 3, we describe differences between fluid flow in straight and curved channels. The flow is effected by several competing forces responsible for particle mixing, the formulas you can find in this part. Thanks to the right setting of the fluid velocity and forces inside we are able to separate particles.

Next, in Chapter 4, we focus on the model itself. Before creation the best microchannel for our purpose, some drafts were needed. We propose a periodical simulation based on particle reseeding. We analyse several drafts of the channel and move the fluid flow by two different possibilities inside. We analyse also fluid flow with immersed particles and compare particle trajectories. Based on the results, we were able to choose the best possibilities for computational studies next.

In Chapter 5, we show three different geometries: torus, cylindrical annulus and helix. At the beginning we briefly describe an implementation of analyzed geometries in ESPResSo. We analyze Dean effect and Dean vortices in cross-sections and the fastest velocity flow in simulations without particles immersed. We need to know wheather the fastest flow is influenced also by other parameters that are considered and compared.

Chapter 6 covers analyses of Dean effect with two types of particles immersed. We compare three different cross-sections of the channel. Focusing length, fluid velocity and particle size are analyzed there because these parameters influence results the most. We mainly focus on particle focusing performance to get the best separation potential. At the end of the chapter we compare our computational results

with the results published in literature, which we used for our microchannel geometry design at the beginning of our research.

In Chapter 7 we describe the first draft of adding some roughness elements to the channel walls. We compare Dean effect in cross-section of square serpentine channel without and with roughness and analyse the effect of roughned walls to the Dean vortices.

Finally, in Chapter 8, we summarise the contributions of this thesis. We add future goals and closing remarks to the end. The chapter is completed by list of the published and submitted papers.

Parts of this work have been published in the publications listed in Section 8.3 and are reproduced here with permission of the coauthors and in accordance with publishers' policies.

2 Current state-of-the-art

Based on the article [35], with a suitable geometry of the curved channel, it is possible to sort the cells according to their sizes, thanks to their tendency to approach the inner or the outer edge of the channel. If we use a curved microchannel, we can observe a kind of secondary flow that is perpendicular to the main flow in the cell trajectory. This secondary flow is caused by the Dean effect, which is related to the inertial force acting on the fluid. One of its many uses is mixing objects with different sizes in a given channel [35].

In biomedicine overal, inertial effects have found their usage in practical applications, e.g.recovery of rare cells from blood [29], separation of particles by deformability for instance diseases red blood cells from healthy ones or search for sepsis markers [12]. Subsequently, many research studies were focused to understand the underlying physics of this phenomenon through experimental studies, theoretical analyses and numerical simulations [25, 6, 14].

In recent years, a wide variety of devices for cell sorting and separation based on such inertial effects have appeared. Most of these devices are designed under the assumption that a secondary flow appears in curved channels, which is also dependent on the setting of the flow velocities as well as the curvature of the channel [10]. In this paper, the authors investigate the centrifugal forces acting on the fluid creating the pressure difference between the inner and outer bends of the tube. This pressure difference leads to the creation of a given secondary flow. Different curvilinear channel geometries are used in the devices to allow a given secondary flow to occur and to ensure the possibility of cell sorting. Prototypes of curved microchannels are used to separate particles with a specific size based on inertial flows in biological samples. However, determining the optimal channel dimensions for size-based separation is very challenging due to individual particle interactions and also due to the high sensitivity of inertial forces to channel geometry [9]. Computational experiments are run for different curvatures and cross-section sizes, and simulations

are validated using available experimental data. Optimizing the channel structure is important to improve processing speed and separation. The curvature of the channel improves the quality and the aspect ratio increases the ability of cell separation in curved channels [9]. In the article [34] we can read about the mixing of particles in microfluidic devices and how these devices present a challenge due to laminar flows in microchannels, which are the result of a low Reynolds number determined by the hydraulic diameter of the channel, the flow velocity and the kinetic viscosity of the fluid.

Next interesting phenomenon describes an article [11] about effects of different roughness elements on friction and pressure drop of laminar flow in microchannels. The surface roughness can have a specific effect on flow performance in microchannels. This paper aims to investigate the different roughness elements on microchannel walls and changes in elementary geometry and flow conditions. Results show a significant effect of roughness on the pressure drop and friction.

2.1 ESSPResSo and PyOIF

The continuous simulation of the flow of elastic objects in a fluid is enabled by the open-source software ESSPResSo, more details in [7]. It is used for various simulations of soft matter in physics, chemistry and molecular biology and contains many advanced simulation algorithms. It focuses mainly on molecular dynamics, but it can also effectively simulate microscopic elastic objects.

In addition to the development of this software, the Cif-BMCG research group is also involved in the implementation of the PyOIF (Python Object-in-fluid) software package for this software. PyOIF is capable of simulating flow of elastic objects immersed in a fluid, widely blood cell suspensions. The module is based on a two-component model of fluid and immersed objects.

The calculation module is programmed in C++. It is used to simulate elastic objects immersed in a liquid. We use the Python scripting interface for running simulations, storing and processing data, as well as for rendering. This software implements a cell flow model based on three main components: a fluid model, models of several elastic objects and various types of interactions. We focus on the elastic objects and their interactions with surroundings, since that is the part of the model that we have used, and we put also little bit more emphasis on the fluid model, since the fluid flow with particle immersed in, is the primary subject of our research.

2.1.1 Simulation box

First of all, there is a simulation box need to be defined at the beginning of every simulation. We do it by define boundaries. It is done using geometrical shapes in ESSPResSo such as rhomboids and cylinders (the most often), but there are also other boundary types available. If it is needed, we can define also obstacles to the simulations, but this is not a goal in this work. Our simulations are simulated with time step of 0.1 μs, it means one step in the simulation represents time 0.1 μs.

2.1.2 Fluid model

Once the obstacles for simulation box are created, we need to fill the simulation with the fluid. The fluid is modeled using the Lattice-Boltzman method [7]. It is discretized by an Euler grid and the flow of this fluid is calculated at its individual points. The fluid is represented by fictitious particles, and each particle contains information about the speed and direction in which it moves. Individual particles bump into each other and transfer energy to each other. The fluid volume is discretized into a three-dimensional grid, we use the D3Q19 version, which has 3 dimensions and 19 discretized directions.

There are two ways the fluid can be moved in the software ESSPResSo:

Type 1 **External force density**

> The first way is to define an external force to each discretization point of the fluid grid, which we set with the external force density parameter.

Type 2 **Moving boundary**

> The second way is to use constant Dirichlet boundary conditions at a concrete boundary with a certain speed, which gradually moves the liquid. This boundary can be either a wall element or a specific obstacle, with predefined constant values field at the boundary points. In our case the wall has the shape of a rhomboid.

2.1.3 Object model

The elastic object model was developed mainly for modeling red blood cells, but it is also possible to model objects of other shapes. In the model, the object membrane is represented by triangulation of its surface. The elastic properties of the object are ensured by five elastic modules. Individual modules have a defined force acting on the vertices of the network. The size of the force depends on the size of the relevant elastic coefficient for the given module and on the change in the position of the peak.

The **modulus of elasticity**, denoted **ks**, describes the stiffness of the object. At the moment when part of the membrane is stretched, this module ensures its effort to prevent this change. We can think of the edges of our triangulation as springs that want to maintain their rest length.

The **bending modulus**, labeled **kb**, is also involved in maintaining object shape. However, it represents a different component, its mechanism is responsible for preserving the angles between adjacent triangles, which keeps the object in its relaxed shape.

The **local area preservation module**, labeled **kal**, already suggests from its name that its task is to preserve the area of individual triangles in our triangulation. This module performs somewhat similar mechanisms to the elasticity module.

The module for preserving the **total area**, labeled **kag**, is among the modules ensuring the global properties of the object. In the real world, the object retains its surface, so this module does not copy any measurable mechanism of the object, unlike the previous modules, where one can observe and measure, for example, the speed of returning to the original state under the action of various forces.

The last module is the **volume conservation module**, labeled **kv**, which is responsible for the object maintaining its constant volume. Again, this global module is not specifically tied to a particular biophysical mechanism. In reality, the object maintains a more or less constant volume and major changes occur only in the very specific and unique situations.

The initial geometry of each elastic object is defined in two files: nodes, that contains coordinates of the mesh points and triangles, that contains triangular incidences. Because the red blood cell is elastic and easily deformed, we will use spheres for our purpose at the beginning of our research.

- **Sphere**

Sphere is based on the discretization of their surface with an irregular triangular mesh, see Figure 2.1. Inside the objects there is the same liquid as in their surroundings. In this thesis we use stiff spheres.
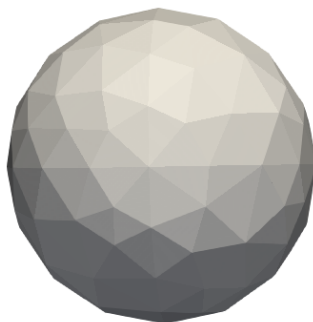
Figure 2.1: Sphere.

We set the modules according to Table 2.1. When we simulate fluid flow with particles immersed, all of our simulations are simulated with stiff spheres. We wanted to avoid problems with the elasticity of real red cells and other elastic components in the blood at the beginning. Elasticity and object deformations are not our goal in this work.

Elasticity modulus	Bending modulus	Local area modul	Total area modul	Volume conservation modul
ks	kb	kal	kag	kv
1	0	0	0	0

Table 2.1: Shpere parameters.

2.1.4 Interactions

The objects can deform and also interact with the fluid due to the fact that the surface of the objects is discretized by a triangular mesh. Interaction is provided using the method of nested objects. Interactions between object models and interactions between objects and fluid are also very important for research purposes. It is also important to take into account interactions between other objects present in the simulations, such as the channel walls themselves, or various obstacles in the channel.

There are three types of interactions.

- **Object-object interactions**

Since we have two or more objects, we can also set up the object-object interactions so that they know about each other. For our simulations needs, we use 58 spheres in every simulation. When they are seeded to the channel, they look like a group of spheres, see Figure 2.2.
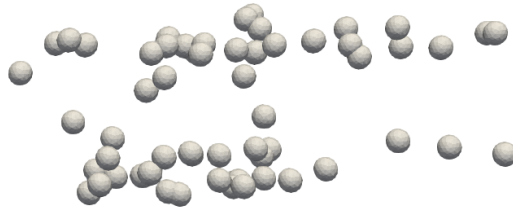
Figure 2.2: Group of spheres.

These interactions act pointwise, e.g. each particle of type 0 (all mesh points of object 0) has a repulsive membrane collision interaction with each particle of type 1 (all mesh points of object 1) once the pair gets closer than membrane-cut, see [17]. This interaction serves so that the grids of the two objects overlap when they collide, but bounce off each other.

We did not set up interactions between them, because they are distributed from each other across the x-axis and also across the y-axis and we do not have to do it. After the beginning of the simulaion, the objects are distributed far away from each other.

These models and their implementation in the ESPResSO software are also explained in more detail in [7].

- **Object-boundary interactions**

These interactions is implemented for contact between objects and walls of the simulation channel, or between objects and other solid obstacles in the channel. These interactions are also pointwise, e.g. each particle of type 0 (that means all mesh object points) will have a repulsive soft-sphere interaction with all boundaries of type 10 (here all boundaries) once it gets closer than soft-cut. The parameters soft-a and soft-n adjust how strong the interaction is and soft-offset is a distance offset, which will always be zero for our purposes [17]. The repulsive force acts on the

points on the surface of the object only if their distance to the obstacle is less than the threshold value, which enters as a parameter in the setting of the interaction forces between the nested object and the obstacle.

- **Interaction of the object surface with itself**

When the object bends and different parts of its surface come into contact, this interaction is important. In such a case, it is necessary to prevent the object from folding over itself, and this is ensured by the presence of the interaction of the object surface with itself. This interaction is implemented in the same way as the interaction between object and other objects.

2.2 Hardware and supporting software

A Dell Latitude 5590 personal laptop was used to run, process and analyze the simulations. As the simulations started to be time-consuming later, we often used a remote Snorlax computer machine to run more simulation batches in one time or to run long-time simulations during the night, thanks to more cores in. To visualize the simulation results, we used the software Paraview [27], where the most of our pictures in this work were done and the generated VTK files [33].

ESPResSO and PyOIF

In this work we use last version available on github [5]. PyOIF is a computational module, we use last version PyOIF 2.1.

The parameters of individual machines are as follows:

Dell Latitude 5590
Personal notebook
Procesor: Intel(R) Core(TM) i7-8650U CPU, 1.90 GHz, 2.11 GHz
System type: x64-based processor
RAM: 16 GB
SSD: 256 GB

Snorlax

Computer financed by the Slovak Research and Development Agency project (project number APVV-15-0751)

Processors: AMD Threadripper 2950X - 16/32T-Core, 3.5 GHz (180W), Boost 4.4 GHz

SSD: 1 TB NVME

HDD: 8 TB

GPU: GTX 1080 Ti

For better image about individual machines in real time, there is a table with a relative comparison of the speed of the machines that were used during the simulations, so the use of the Snorlax machine generally accelerated the experiments that ran on a Dell laptop and also how long the shortest and longest simulations took. Specific values of the inlet conditions and the corresponding flow rates are presented in Table 2.2. Results in the table are approximatelly. We can see, the simulations on a laptop take almost twice as long as on a virtual machine.

Machine	Computation time [hours]	Average velocity $[\mu m/\mu s]$
Snorlax	4.5	0.18
Snorlax	2.7	0.6
Dell	7.8	0.18
Dell	4.5	0.6

Table 2.2: Comparison of machines.

3 Inertial effects in curved channels

Flow in microchannels have similar characteristics based on their shapes. In addition to straight channels, there are several types of curved microchannel structures: curved serpentine channels, spiral channels, square serpentine channels, etc. These structures were created to introduce extra inertial effects, such as Dean flow, to achieve manipulation of particles.

This chapter covers theoretical basis about inertial effects in microchannels, because if we want to simulate the fluid flow in our best, we should simulate also inertial effects in connection with curvature. Parts of the Section 3.2 were publicated in a paper [3] as a part of conference.

3.1 Straight channels

When we imagine a simple straight microchannel with a fluid flow, submerged particles move almost in a straight line in it. The fastest flow in such a channel is located in the middle of the cross-section, along the main axis. Fluid flow is characterized by its parabolic shape in the velocity profile in the cross-section. It is called Poisoeuil's flow, see Figure 3.1, more you can find in [7].
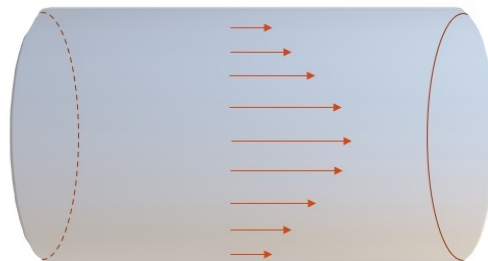
Figure 3.1: Parabolic shape in fluid velocity profile in the cross-section of straight channel, named Poiseuille flow.

The Dean effect described in 1.1 does not appear in the direct channel. In the paper [13] also states that, in general, the Dean number in a straight channel is zero, which means that there is no Dean flow in a straight channel in the laminar flow state. Straight channel comprises only two competing forces in main axial direction: wall interaction lift forces and shear gradient lift forces, see Figure 3.2. More about these forces and their formulas will be discused in Section 3.2.
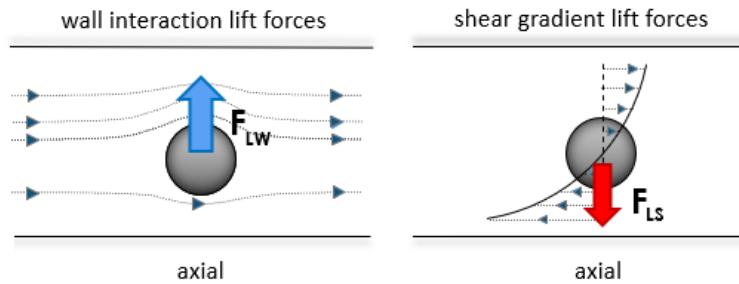
Figure 3.2: Competing forces in straight channel.

Particle focusing in straight channels about 60% away from the tube centerline is caused by a balance of inertial shear gradient lift forces pushing the particles towards the wall and a wall repulsion forces caused by an increased pressure between the particles and the wall [24]. Inertial migration is a phenomenon where randomly dispersed particles in the entrance of a straight channel migrate laterally to several equilibrium positions after a long enough distance [39]. According to the article [13], the final equilibrium position of particles in straight channels depends on the shape of the channel. In them, the particles move to several stable positions depending on the cross-section of the channel. Figure 3.3 shows 4 different cross-sections of the channel and the resulting stable positions of the particles in their flow. In the case of particles moving in the flow of a circular channel, their stable positions were formed over time by an intermediate circle due to the circular cross-section (Figure 3.3 (a)), due to symmetry of the circle. For a square cross-section, particles moving in a channel of square cross-section are located in four equilibrium positions close to the center of the channel (Figure 3.3 (b)). In a rectangular channel, the particles are finally situated in two equilibrium positions near the center of the long channel wall (Figure 3.3 (c, d)).
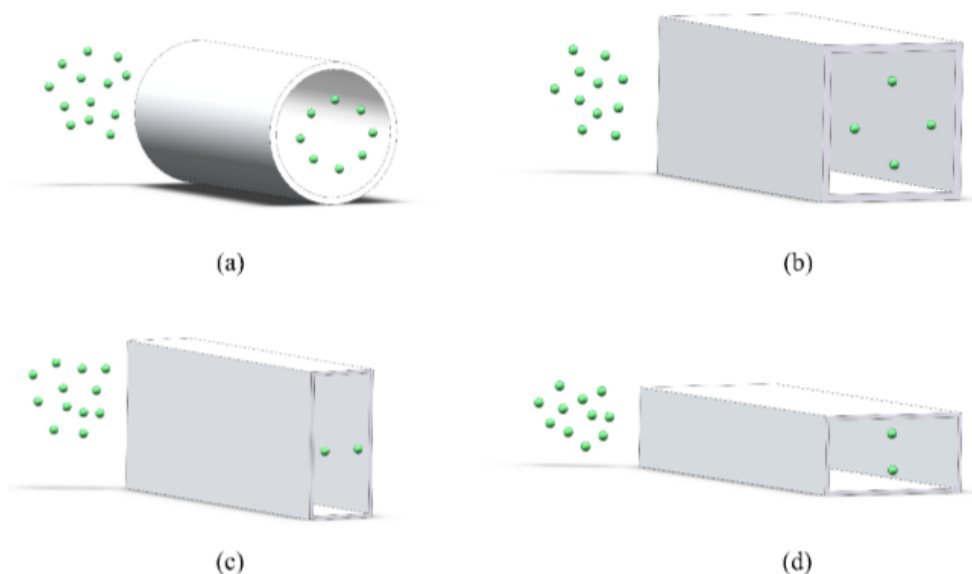
Figure 3.3: Schematic of the focusing position of particles migrating through channels with different cross-section shapes: (a) circular channel; (b) square channel; (c) high-aspect-ratio rectangular channel; (d) low-aspect-ratio rectangular channel, reprinted from [13].

However, such particle targeting in straight channels is very slow. It is significantly more efficient in curved channels due to the secondary Dean flow.

3.2   Curved channels

In curved channels, the movement of the fluid is not the same like in straight ones. Due to the curvature in the channel, a centrifugal force acts on the fluid and causes non-zero velocity deviations in the transverse direction. This centrifugal force also depends on the speed of the flowing fluid, which causes the centrifugal force to be greater in a faster flow. When we insert some solid particles into a curved channel with fluid flow, the trajectories of individual particles will deviate to the walls as a result. We expect a deviation towards the outer or inner wall of the channel, depending on the size of the particles in the flow. This behaviour causes the Dean effect. The analysis of fluid flow in curved channels and immersed particles will be discussed in detail in Chapters 5 and 6. The forces responsible for such deflection like focusing particles on channel walls are threefold: the wall interaction lift forces, the shear gradient lift forces and the secondary-flow induced Dean drag forces, see Figure 3.4. As the streamlines are diverted toward the side of the particle away from the wall,

the fluid accelerates, causing low pressure on the top and higher pressure on the wall side of the particle, which generates the wall interaction force, Figure 3.4 on the left.
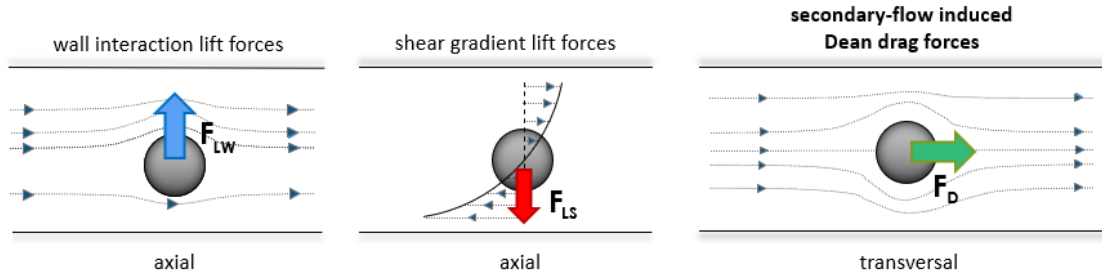
Figure 3.4: Competing inertial forces in curved channel.

The formula giving the magnitude of the wall induced force is

$$F_{LW} = C_W \rho U_{max}^2 a^6 / D_h^4, \tag{3.1}$$

where C_W is a lift coefficient dependent on particle position and on Reynolds number [8], ρ is the fluid density, U_{max} is the maximal fluid velocity, a is the particle diameter, and D_h is the hydraulic diameter of the channel.

A typical microfluidic velocity profile is parabolic and, thus, curved. A particle at a position in such a flow will experience velocities of different magnitudes on either side. The fluid flow around the particle must compensate for this difference and induces a force on the particle directed toward the side of the particle with a higher relative velocity (normally toward the walls of a microfluidic channel or areas of increasing shear), Figure 3.4 in the middle. This shear induced lift force has magnitude

$$F_{LS} = C_S \rho U_{max}^2 a^3 / D_h, \tag{3.2}$$

here C_S is a shear coefficient dependent on particle position and on Reynolds number [8].

In curved channels, the centrifugal force generates a secondary flow that is perpendicular to the main flow direction. Normally, this flow is two orders magnitude weaker than the main flow, however it is sufficient to create the drag around the particles causing transversal motion across the cross-section, Figure 3.4 on the right.

The formula for the evaluation of Dean force takes the form

$$F_D = 3\pi\mu a U_D, \tag{3.3}$$

where μ is viscosity of the fluid and averaged Dean velocity can be approximated by [26]

$$U_D = 1.8 \cdot 10^{-4} De^{1.63}. \tag{3.4}$$

Here, De denotes Dean number given by

$$De = Re\sqrt{\frac{D_h}{2R_c}} = \frac{\rho U_{max} D_h}{\mu}\sqrt{\frac{D_h}{2R_c}}, \tag{3.5}$$

Re being the Reynolds number and R_c the curvature radius of the channel.

The interplay between the wall and shear induced forces and the Dean force determines the cross-sectional trajectory of a particle. There are however numerous assumptions for the validity of provided formulas, such as straight channels for lift forces and curved channels for Dean forces, which are not possible to be met simultaneously. Also, position dependent coefficients C_S, C_W cause the evaluation of the forces difficult. Therefore the actual simulations of the channel flow with immersed particles are extremely useful for studying the stabilized positions after focusing.

4 Channel geometry

In this chapter, we describe microchannel creation process. We start with proposals of several geometries. We compare them and try to create the best one for our purpose. We discuss some problems with EspreSSo package and limitations there. As the right geometry for the simulations is crucial for particle separation, the development of it and designing of it were hard and took a lot of time at the beginning.

4.1 First draft

Within microfluidics, there are numerous concepts for geometries, like we described in Section 1.2. As we mentioned in the 1.1 section, the main reason for using a spiral microchannel is the separation of small and large components in the fluid. In numerical simulations, however, it is computationally and time-consuming to simulate the entire device. We are not able to build a long spiral of such a scale where we could study the mentioned Dean effect. Therefore, we constructed a closed geometry and used only a certain section of it, thereby approximating the simulation of only part of the device and simulating the fluid flow into it. Thanks to the ability to move particles within a given geometry, which I will describe below, we were able to investigate the Dean effect by simulating uninterrupted fluid flow. The stable positions of the particles do not change over time in such a simulated flow. Likewise, the properties of the fluid flow do not change over time.

To investigate the Dean effect, we initially chose a geometry in the shape of a racing track as a first draft. We can see it in Figure 4.1. We created it using blocks. We moved the fluid in the left part of the geometry, where the inserted cuboid can be seen in addition. It is one of the ways to move the fluid in simulations. Nested objects are characterized by boundaries that contain a set of boundary points. These boundary points are moved by the force that arises as the interaction of the fluid

with the elastic-mechanical properties of the nested object. The nested boundary of the object has the same speed as the fluid speed. But the block has a constant speed along its entire surface, which is unphysical. This phenomenon can be seen in Figure 4.2. In the left upper part of the track, the velocity boundary generates horizontal flow that is constant on the surface of the boundary, however after a short distance, the flow becomes parabolic. The solution is therefore, let some section of the channel fluid flow freely so that the flow stabilizes and the Poissoeuil's parabolic shape establishes in the velocity profile in the cross-section of the channel as we mentioned in Section 3.1. This is the reason why we use straight part of the channel before the curve section. This parabolic shape in the velocity profile is also necessary in curved channels.
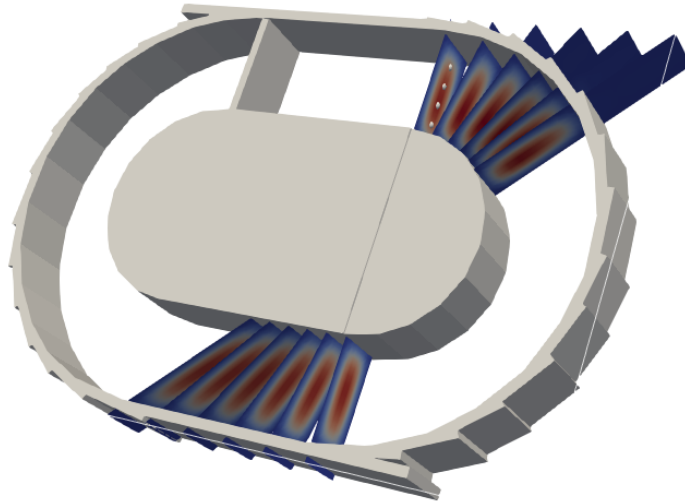
Figure 4.1: First draft of the curved channel.

4.1.1 Particle seeding to first draft

To simulate a continuous serpentine-like curved channel, the particles need to be reseeded only in the curved section of the track. So we placed the particles at the beginning of the curved section of the channel. The seeding position in indicated by line 1 in Figure 4.2. In the Figure 4.1, it is the first cut, which we called the starting or seeding line, and it contains four particles of the same size with a spacing of 10 micrometers.

Subsequently, we observed the individual cross-sections of the channel (visualized in Figure 4.1) and the particles in it and recorded the position of the center of each of them. We then created trajectories of their movement from the distance between the center of the particles and the inner edge of the channel. In addition, we monitored the distance of the center of the particles from the inner edge of the formed channel and analyzed the gradual deviation from the initial distance. The simulation was time-consuming and took a long time due to the elongated part of the channel in the location before the baseline for particle placement. In order to save time and therefore to shorten the simulation time, after finishing the curvature in the channel (at the place where the first cut ends in Figure 4.1), we placed a reseeding line. The reseeding line is indicated by line 2 in Figure 4.2. From this moving line, we moved the particles back to the seeding line 1. When relocating, we preserved the exact distance of the particles from the inner edge as well as the rotation of the particles and continued the simulations and tracking the trajectory of the particles embedded in the flow.

To summarize, in Figure 4.2 you can see 2D view of the first draft of our microchannel geometry. We can see here seeding line (number 1 in graph), reseeding line (number 2), visualisation cut (number 3). Before entering the curved part in the channel, we have a straight part for stabilization of the fluid flow to get the parabolic shape in fluid velocity profile in the cross-section of straight channel, named Poiseuille flow, discussed in 3.1. Then we immersed particles to the seeding line and recorded the fluid flow. We kept track of the positions of the centers of the particles relatively to the channel cross-section. This gives us information how particles move across the cross-section. Trajectories were then analyzed and compared.

In Figure 4.2, in addition to individual particle trajectories, we have the opportunity to see the positions of four particles in the first step of the simulation (on the starting line, where we first placed the particles) and also the positions of the same particles in the hundredth step of the fluid simulation a little further. We can also notice that each particle has a different trajectory length and therefore reaches the displacement line at a different time. In addition to the starting a replacement line, the visualization location is also shown in this image. This is a cross-section of the channel in which we subsequently observed the Dean effect.

Figure 4.2: 2D view od the first draft of geometry with four particles.

By running the simulation with the given channel geometry with four nested objects of the same size, we obtained four resulting trajectories. Figure 4.3 shows the first 1000 steps and the distance of individual particles from the inner edge of the channel. It can be seen from the graph that the particles started to deviate from their original position at the beginning of the simulation towards the outer edge of the channel. But the trajectories are not periodical, we observe there **particle re-seeding artefact**.

4.1.2 Particle re-seeding artefact

In addition, however, we can observe unexpected peaks for each trajectory. They are caused by moving particles from the reseeding line to the seeding line, defined in channel geometry. To explain this re-seeding artefact, we need to look on local velocity field along the seeding and re-seeding lines 1 and 2 and the line 3 in Figure 4.2. While the velocity flow near line 3 is curved both before and after the line, at lines 1 and 2, it is curved only on one side of the line. Therefore locally, the fluid along lines 1 and 2 does not resemble completely curved flow as was the original intention mentioned in the begining of Section 4.1.1. This cause the peaks in particles' trajectories.
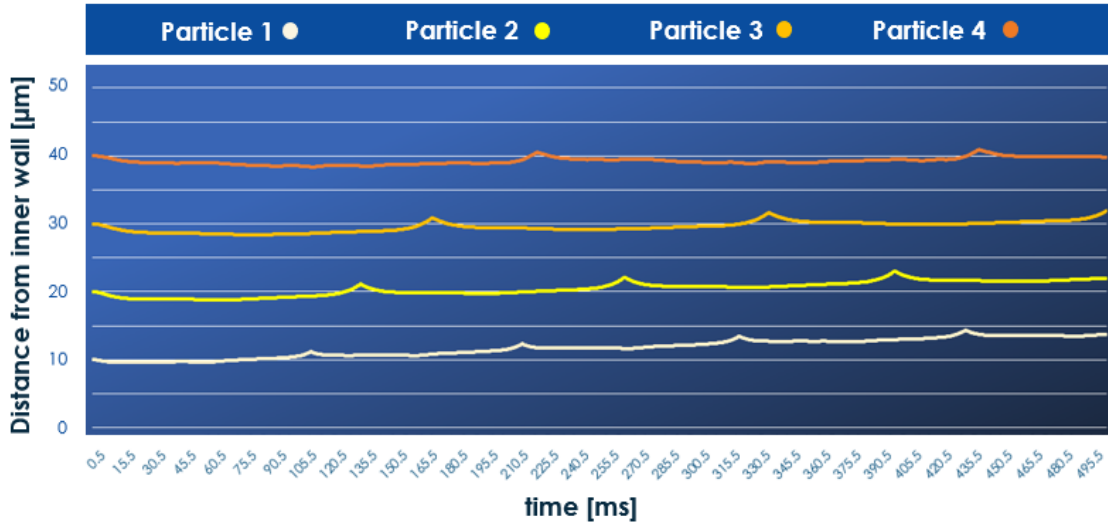
Figure 4.3: Particle trajectories during first 500 ms of the simulation in first draft geometry.

4.1.3   Cylindrical ring with square cross-section

Thanks to the analysis of the fluid flow and particle trajectories, we realized that the geometry was unnecessarily elongated, which caused the simulations to take an unnecessarily long time, since the fluid flow was stabilized after the first few steps. In this case, the flow is already steady after $50\mu m$ (about one channel width) and a parabolic velocity profile is already established. We found that we can omit the straight parts of the channel before the starting line from Figure 4.2. Moreover, the straight channels cause the peaks. Therefore, we modified the proposed geometry. We shortened the part of the channel in front of the seeding line for the placement of the particles and in addition we widened the channel. We thus obtained shorter simulation time because in turn it reduced the time needed to run the simulations.

In Figure 4.4, we can see the new channel geometry constructed in this way. We did it by two circles and we simulated the flow between them, so we created a cylindrical ring with a square cross-section. Again we seeded four particles on the seeding line and watched the positions of particle origins during the flow. When the particles arrived to the reseeding line, we reseeded them back to the seeding line with new coordinates of their origins and we continued by watching and recording the particle origins. With this kind of reseeding we did a simulation of periodical

49
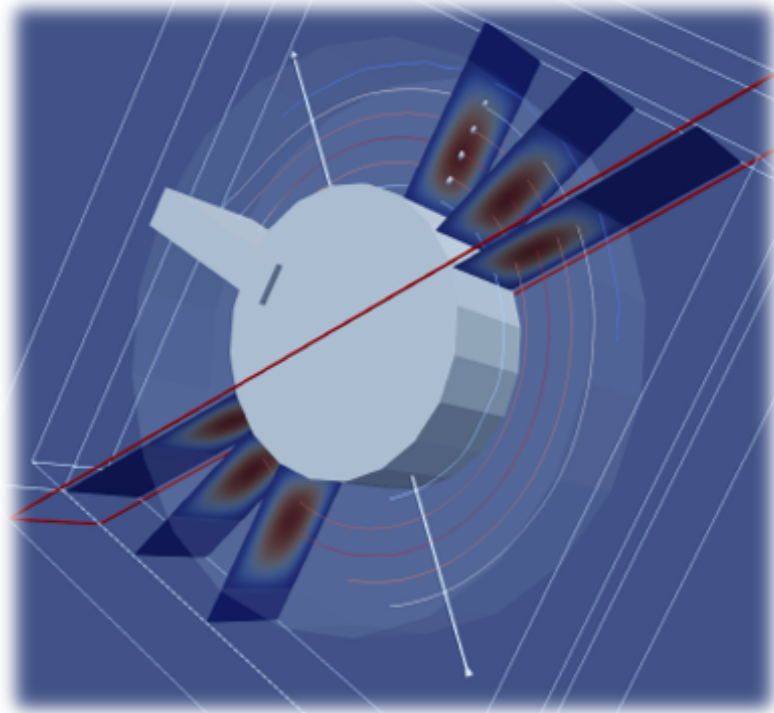
Figure 4.4: Cylindrical ring with square cross-section. Four particles are seeded there.

flow without real construction of the real microchannel. The velocity cube for moving the fluid flow to the left as far as possible from the visualization point, which we left between the seeding and reseeding line.

When running the simulations without particles immersed, we changed the fluid flow parameters as well as the channel settings. In the Chapter 5, where we analyse Dean effect in three different geometries without particles, we can see how individual parameters and settings affect the Dean effect a Dean vertices in cross-sections.

For Dean effect analysis with the particles immersed, we seeded four particles to the simulation. Distance between the centers of the spheres were always $10\mu m$. We analysed three types of size ($2\mu m$, $4\mu m$ and $6\mu m$) with the same fluid velocity. The initial seeding to the cylindrical ring with square cross-section you can see in Figure 4.5 for every case.
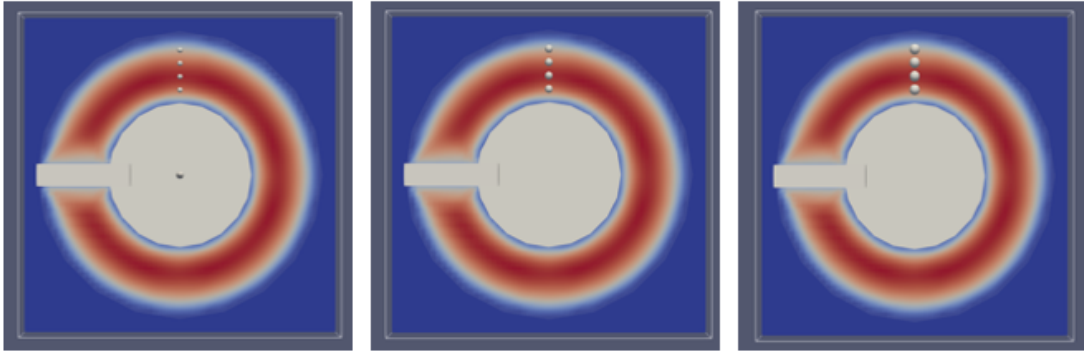
Figure 4.5: Particle seeding in simulations for particles of three different size (smallest, middle and largest ones).

In the Figure 4.6 we can see the resulting trajectories of three sized particles during first 500 ms. Our analysis of Dean effect in cylindrical ring with particles immersed shows unexpected results, while the Dean effect is too big. It pushes all the seeded particles to the same channel wall after few steps in our simulations.
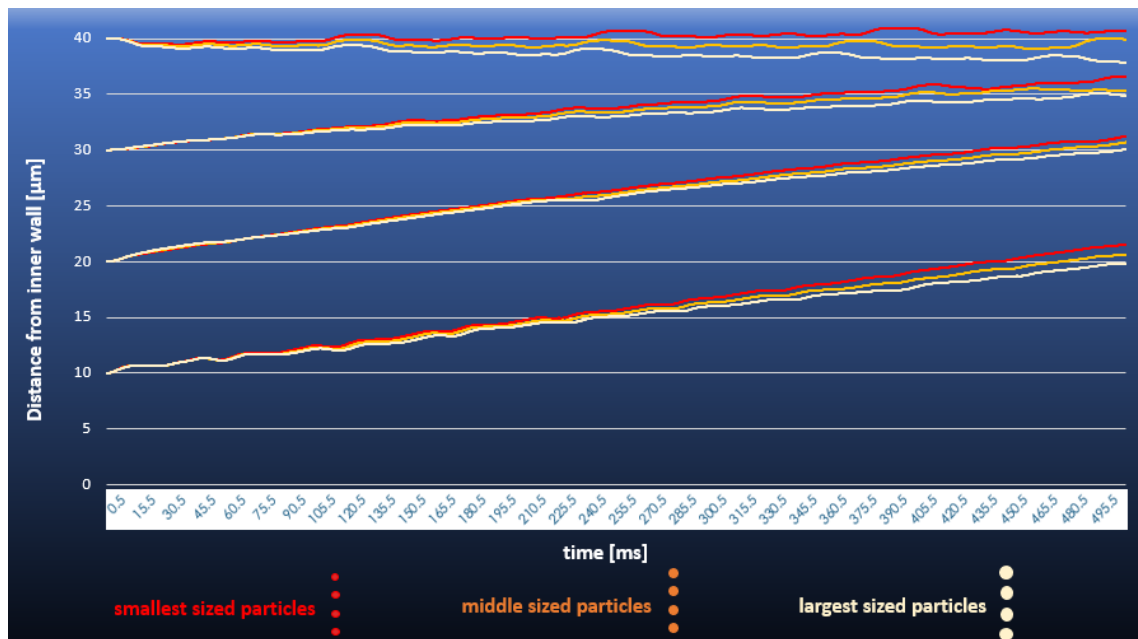
Figure 4.6: Trajectories of three sizes of particles during first 500 ms in geometry of cylindrical ring with square cross-section.

4.2 Second draft

Due to the fact that we wanted to try to reduce the Dean effect, which pushed all the particles to one edge of the channel - to the outer one, we considered the geometry of cylindrical annulus with curvature radius of $3000\mu m$, see Figure 4.7. The reason was that Dean's effect always exceeded the Lift-force effect and the flow did not mix the particles, but only pushed them all to the edge. According to the formula, however, the Dean effect can be reduced in only one way, and that is to increase the denominator, see (3.5). So we increased the radius of the geometry Rc to $3000\mu m$.

Such change however caused the computational domain to become too large. The computer resources are not able to accommodate such large domain. And even if they were, the simuluations of such large channel would last unacceptably long. Therefor we decided to simulate only a part of the channel. So we cut out only this part of the 15 degrees and moved the particles from seeding line to reseeding line with some rotation of those particles, with new coordinates, in order to preserve the periodicity of the flow. The seeding and reseeding lines are depicted in Figure 4.7.

4.2.1 Second draft with external force density

As we mentioned in 2.1.2, we have two possibilities to move the fluid. In case of moving fluid by moving boundary, we would have to put this boundary long enough before the seeding line, so that the fluid flow stabilizes as soon as possible to get the parabolic shape in fluid velocity profile in the cross-section of straight channel, named Poiseuille flow, discussed in 3.1. This could be solved by seeding and reseeding the particles further from the inlet and outlet moving boundaries.

There is however another effect of the moving boundary that defines constant velocity field on its surface. It effects the Dean flow. Since at the boundary, the velocity field is constant, there is no secondary Dean flow. While the parabolic Poiseuille flow establishes quite short after the boundary - approximately in 50 μm - it takes quite long for secondary Dean flow to establish. Therefore we can not use the velocity boundary to move the fluid in this case.
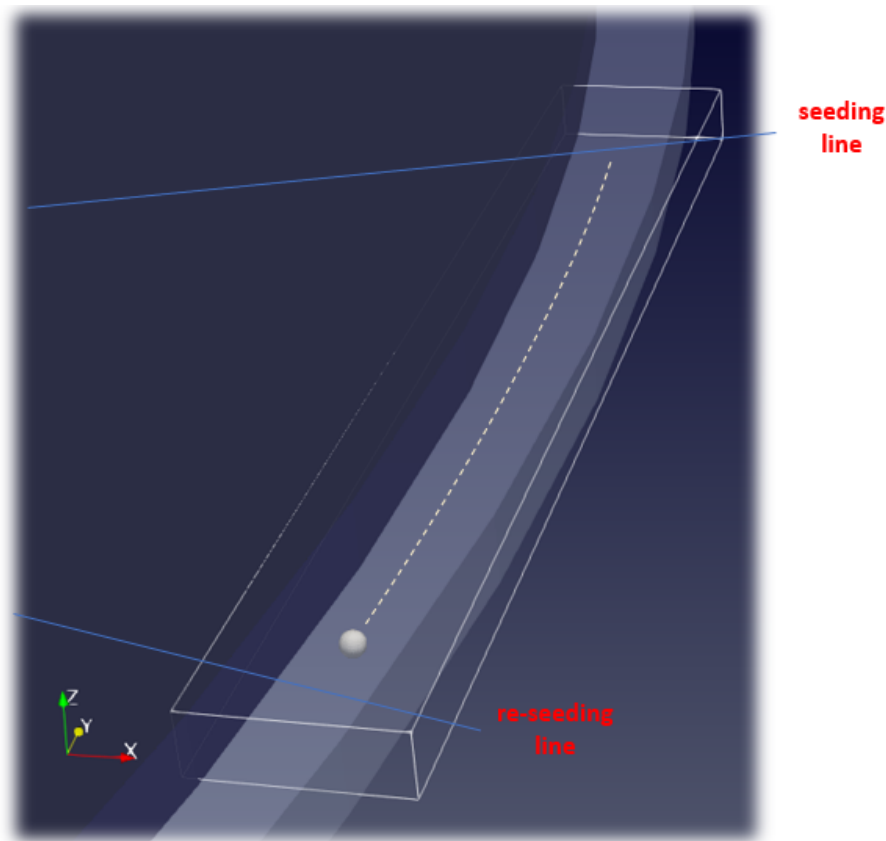
Figure 4.7: Cut of 15 degrees from cylindrical ring with square cross-section with $3000\mu m$ radius.

Since we were not able to move the fluid by moving boundary with ideal conditions of fluid flow, we changed the fluid moving. We tried to run the flow by setting up the external force density. For seeding and reseeding of particles we defined borders like in previous geometries. They are depicted with red colours in the Figure 4.7. The white dashed line shows the trajectory of the particle immersed.

In Figure 4.8 you can see first 678 steps of simulation in 15 degrees cut geometry with particles immersed and fluid move by external force density. Four trajectories of individual particles are depicted here. We can see that particles are pushing to two sides of the channel, one part to the outer wall and second part to the inner wall. This means that we successfully decreased too high Dean effect from previous geometry thanks to 15 degrees cut and thanks to increasing the geometry radius. During the simulations analyses, we again run into a problem with peaks in particle

trajectories, see Figure 4.8.
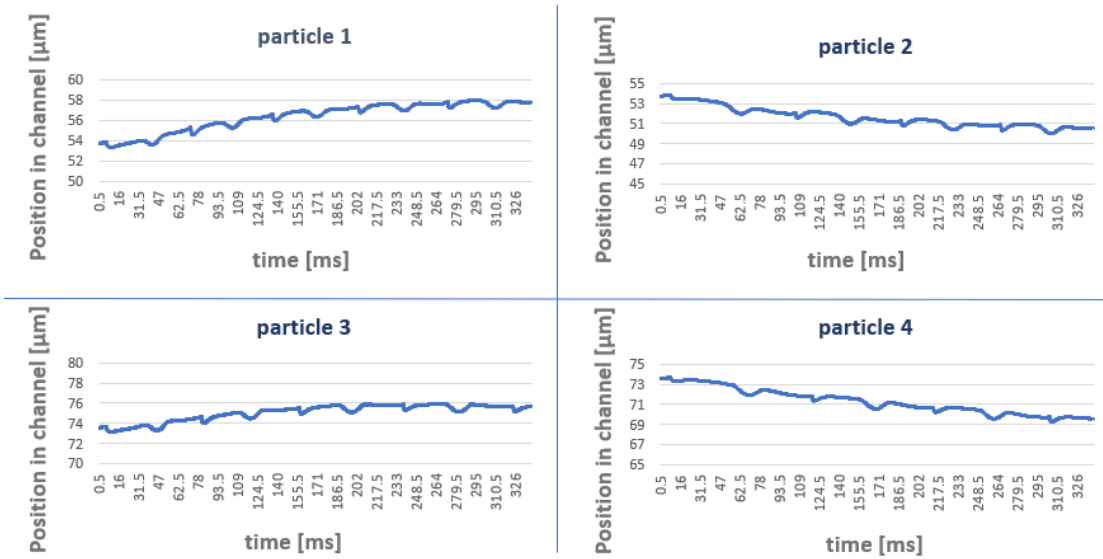
Figure 4.8: Particle trajectories during first 326 ms of the simulation in a geometry of 15 degrees cut with a radius of $3000\mu m$.

4.2.2 Particle re-seeding artefact

Running the fluid by external force density has also limitations in ESPResSo. We defined to each discretization point of the fluid grid an external force. This means, every discretization point has the same force at the beginning.

The reason for peaks to appear is this fact, that the external force density must be defined in ESPesSo constant over the whole domain. In our case however, the flow is curved and thus the force density should also be curved. This functionality however ESPResSo does not offer. As a consequence, the flow in our 15 degrees cut is again not completely resembling flow in a curved spiral and the peaks appear. They are caused by moving particles from reseeding line to seeding line for the purpose of obtaining a periodic simulation.

Since with such curved channels described in 4.1, 4.1.3 and in 4.2 we always encounter the same problem with reseeding of particles, we decided to go in different way in our next research. We decided to change the geometry for particle separation analyses completely. We want to avoid such curved channels and will try to construct a square serpentine channel, more about new geometry one can find in Chapter 6.

5 Analysis of the Dean effect in a fluid

In the next chapter, we focus on fluid flow analysis. First we describe three types of microfluidic channel geometries that we examined. It will be a comparison between torus, cylindrical annulus with squared cross-section, and helix. We ran there simulations without immersed particles to better understand the basic properties of the fluid flow and the Dean effect in it. These properties will have a significant impact on the stable positions of embedded particles in the next part of the research later. In inertial flows without immersed particles, different things are important. In the primary flow, it is the relative position of the maximum fluid velocity with respect to the channel cross-section. In the secondary stream, it's Dean's vortexes.

The most of this chapter was publicated in a paper [21] as a part of conference paper.

5.1 Observed channels

To analyze the Dean effect, we used a torus, which, unlike the square cross-section in the cylindrical ring, has a circular cross-section. It is shown in Figure 5.1. The motivation was to compare the fluid flow in a square and circular channel cross-section. The source of the fluid flow was a circle. We placed it perpendicular to the flow as in the case of the cylindrical ring. We used dimensions corresponding to the dimensions of the channel. The second geometry used in the simulations consists of an annulus supplemented by a third dimension - the height, which together forms a cylindrical ring with a square cross-section, Figure 5.1. The radius of curvature of the ring Rc was measured at the center of the cross-section and varied from 50 to 300 µm in our simulations. The source of the fluid flow was a square source placed perpendicular to the flow, with dimensions corresponding to the internal dimensions of the channel. The last geometry analyzed, which completed the work for comparison, is the spiral with a circular cross-section in Figure 5.1. Details of the

construction can be found in 5.1. The motivation for analyzing the geometry of the spiral is the possibility of manufacturing this device in cooperation with colleagues from the University of Žilina.
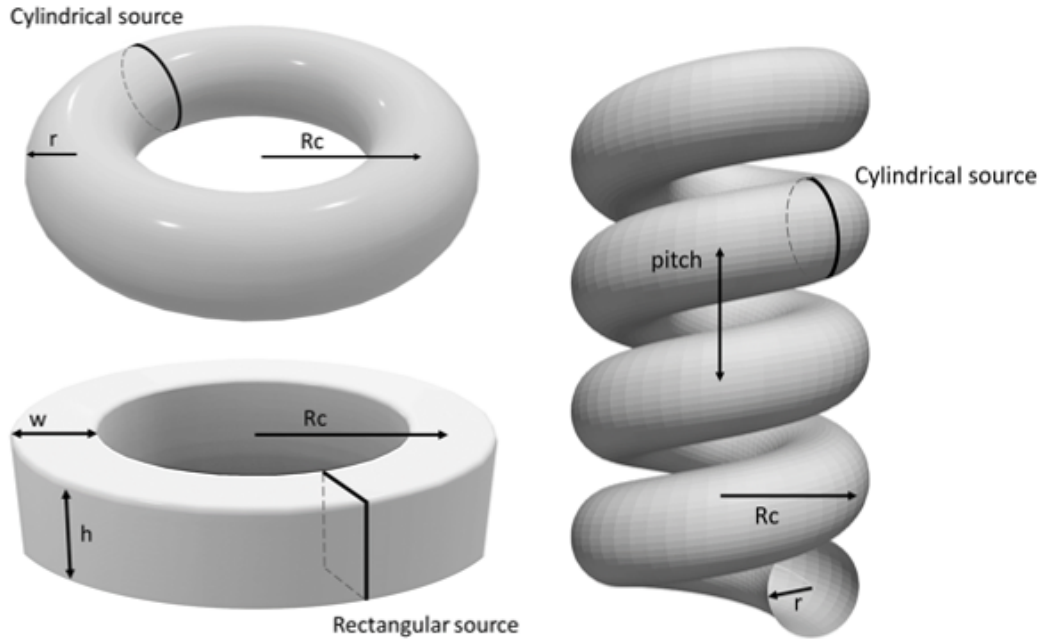
Figure 5.1: Three different channel geometries: torus and cylindrical annulus on the left side and helix on the right.

Implementation of the helix boundary in ESPResSo

In ESPResSo, there are several types of obstacles available. We need to add a novel spatial function defining the helical shape. The question arises - why we did not use a superposition of several simple existing rhomboids to prepare more complex geometry, as the helix is? In that case, we would need a lot of small rhomboids, and the problem with this approach is a non-negligible time needed to incorporate all of them. The initialization of boundary conditions would take several hours this way, [22].

An obstacle in ESPResSo is defined by its surface boundary. The direct definition includes a spatial function defining in the distance of any fluid discretization point to the closest boundary surface. The distance can be either positive or negative, depending on the position of the point, whether it is situated inside or outside of the obstacle.

At the beginning of the simulation, the program defines the boundary conditions – if there are several obstacles, we need to define for each discretization fluid point the distance to the closest boundary.

To evaluate such spatial function for helix, we need to know as input parameters the curvature radius R_c, the cross-section radius r, the *pitch*, and the dimension of the fluid discretization. The axis of the helix is fixed to be the z-axis, and the orientation of the helix is fixed to be the right-handed.

We need to evaluate, for any point with coordinates $[x_p, y_p, z_p]$, the closest distance to the helix. This problem cannot be solved explicitly, since we would arrive to a parametric equation of type $A \cdot sin(t) + B \cdot cos(t) + C \cdot t + D = 0$ for t as unknown variable. This equation can be solved numerically for a given values of A, B, C and D, but cannot be solved for A, B, C, D as parameters dependent on geometrical parameters R_c, r and *pitch*.

For this reason, we do not evaluate the values of spatial function explicitly, but we do it with a numerical calculation.

We are looking for a minimum of functions

$$D_{axis} = \sqrt{(x_p - R_c \cdot sin(t))^2 + (y_p - R_c \cdot cos(t))^2 + (z_p - \frac{pitch}{2\pi}t)^2} \qquad (5.1)$$

$$D_{boundary} = D_{axis} - r \qquad (5.2)$$

where D_{axis} defines the distance of a spatial point $[x_p, y_p, z_p]$ to a point situated on the local axis of the helix. This point has coordinates $[R_c \cdot sin(t), R_c \cdot cos(t), \frac{pitch}{2\pi}t]$. After that $D_{boundary}$ is the distance of the fluid point to the helix boundary. We know that this minimum can be found in z-range $[z_p - pitch/2, z_p + pitch/2]$.

The length of the local helix axis within this range can be approximately calculated as $L = \sqrt{pitch^2 + (2\pi R_c)^2}$. If the fluid discretization is given by a parameter lb_{grid}, than we can assume that the local helix axis will pass through approximately L/lb_{grid} number of fluid points. This number is multiplied by factor 1.5, and the result is used as a number of iterations needed to evaluate the distance of a point

to the closest boundary. The length of the local axis within the considered range is divided into $1.5 \cdot L/lb_{grid}$ segments, and the distance between these segments and the fluid discretization point $[x_p, y_p, z_p]$ is calculated for each of the segments. Finally we keep the smallest distance. This iterative procedure is made for every fluid discretisation point.

More about this special VDT algorithm you can find in [20].
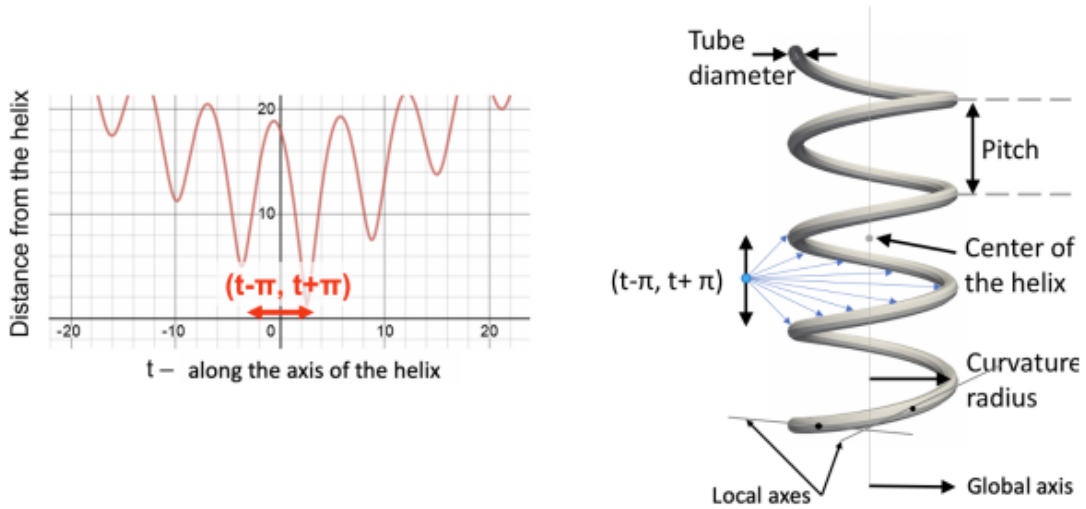
Figure 5.2: The helix boundary point with minimal distance from the space point is within interval $(t - \pi, t + \pi)$. The helix is defined by its center (any point situated at the global axis of helix), its tube radius, pitch and curvature radius.

5.2 Dean vortices in cross-sections

The Dean effect is related to inertial forces acting on fluid in curved channels. Such a channel has a main axial direction in which the fluid moves at high speed. However, several other lower velocities also occur in the transverse direction. This is called the Dean effect and is easily seen when the axial component of the velocity field is removed.

In straight channel in the middle of the cross-section we can observe the fastest flow, along the main axis. The Dean vortices vanishes in the cross-section.

In curved channel, this flow, which was originally in the middle of cross-section, is now pushed to the outer wall of the channel. This is caused by Dean effect. In the Figure 5.3 we can see two Dean vortices in curved channel with circular cross-section. The secondary flow is composed of two symmetrical counter-rotating spiral vortices. Together, these streamlines copy the cross-section of the channel, in this case they copy a circular cross-section.
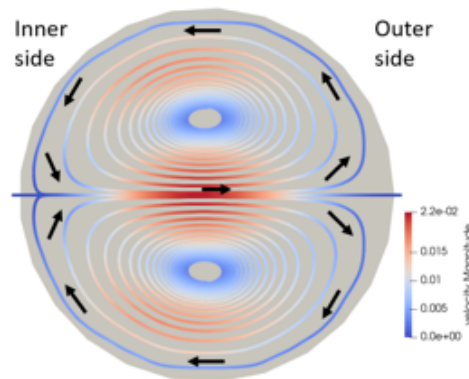
Figure 5.3: Dean vortices in torus with circular cross-section. The colouring is made according to the velocity of secondary flow.

In curved channel with squared cross-section we can see slightly different results. In the Figure 5.4 of a cylindrical ring, we can see the same streamlines projected on the channel transversal cross-section. It is shown as two Dean vortices facing each other, what is similar to what we could see in the case of a ring with a circular cross-section. The coloring is according to the speed of the secondary flow.

Together, these streamlines copy the cross-section of the channel again. In the case of a square cross-section in a cylindrical ring, they create a square together.
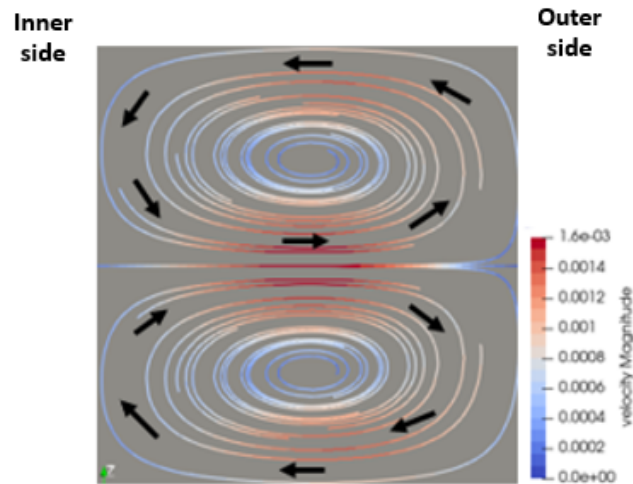
Figure 5.4: Dean vortices in cylindrical annulus with squared cross-section. The colouring is made according to the velocity of secondary flow.

In helical channel it is complicated a little bit. One way how to visualize Dean vortices in spiral channels is to project the streamlines onto a plane that is parallel to the main axis of the spiral, i.e. parallel to the z-axis. This plane is not perpendicular to the spiral, but intersects it at an angle. This angle depends on the height of the pitch in the spiral. At low values of the pitch height, the angle is almost 90 degrees, for larger values of the pitch height, it can be completely different from 90 degrees. You can read more in [31]. The streamlines are not closed vortices, so they are not formed as in a torus or cylindrical ring with a square cross-section. The streamlines are projected like the shapes of the letter S, see Figure 5.5.
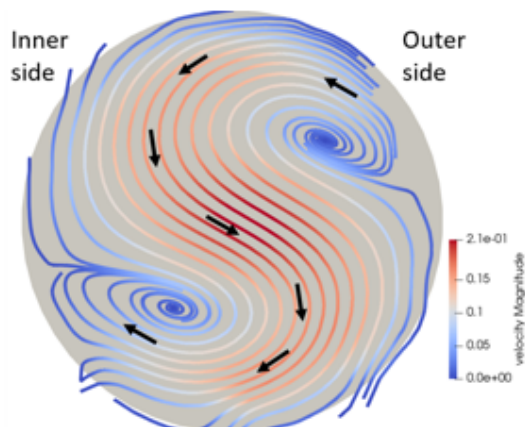
Figure 5.5: Dean vortices in helix with circular cross-section. The colouring is made according to the velocity of secondary flow.

5.3 Results

Our interest in the following subsection was to find out whether the position of the fastest flow in the cross-section of individual selected channels depends only on the Dean's number, or also on other parameters. An overview of all investigated dimensions is given in the Tables 5.1, 5.2 and 5.3. In the following graphs, we show dependence of the position of the fastest flow on the Dean number in channel.

Simulation batch	Curvature radius	Section radius	Fluid aver.vel.	Kinematic viscosity
	μm	μm	$\mu m/\mu s$	$\mu m^2/\mu s$
T1	75	25	0.05 - 1	0.79
T2	75	25	1	0.79 - 10
T3	250	15 - 35	1	0.79
T4	75 - 500	25	1	0.79
T5	75 - 500	25	0.6	0.79

Table 5.1: Investigated geometrical and fluid parameters influencing fluid properties in torus with circular cross-section

The position of the fastest flow was measured as a displacement from the centre of the cross-section. Positive value means deviation to the outer wall of the curvature, the negative number means deviation to the inner wall of the curvature. As an example, the displacement of $-2.5\mu m$ in batch T1 means that the position of

the fastest flow was located $2.5\mu m$ away from the centre shifted towards the inner wall. The precision of the measurements is approximately 1 μm, because the fluid discretization is 2 μm.

In Figure 5.6, we can see the results for simulations in torus. The notation for simulation batches T1 to T5 is the same as in Table 5.1. We can see that tendency of the curves is qualitatively the same. The increasing Dean number causes a shift of the velocity peak towards the outer wall of the channel. However, the absolute position of the curves varies. For example, compare two batches of simulations T4 and T5. The only difference is the value of the fluid viscosity and the difference in the blue and green lines are not only in the shift but also in the slope of the lines. The position of the fastest flow do not depend only on the Dean number.
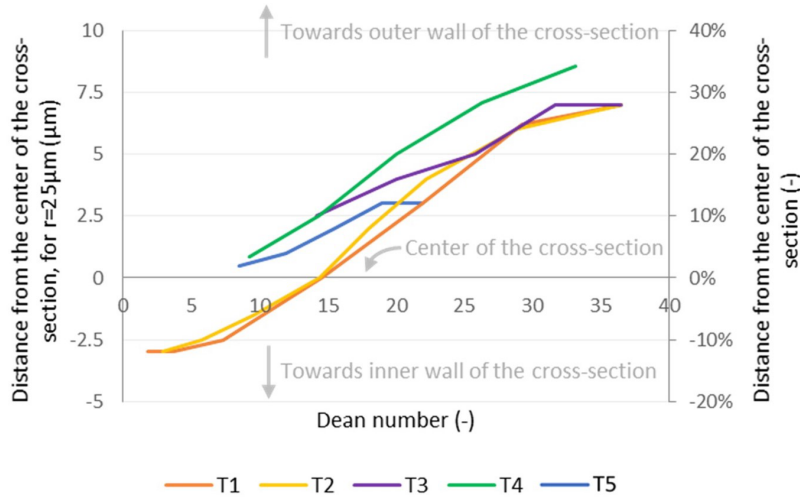
Figure 5.6: Position of the fastest fluid within a cross-section for torus, as a function of the Dean number. Negative values indicate deviation towards inner wall, positive values indicate deviation towards outer wall of the channel. For batch T3, the section radius changes and the absolute distances were replaced by its relative value with respect to section radius.

We can notice that curves T1 and T2 are fitting very well each other. These curves correspond to a set of simulation, where the geometry of the channel was not modified, only the properties of the fluid varied over the simulations. This means, that Re was changed which affected De. For batch T1 we changed the velocities, and for batch T2 we changed kinematic viscosity of the fluid. The other curves, T3 to T5, had a geometry as a changing parameter.

The observation is, that for a given geometry, the position of the fastest flow is dependent only on Dean number. But the relationship is more complicated in case of variable geometry - in this case, it is not only the Dean number that defines the position of the fastest flow.

Simulation batch	Curvature radius	Section square	Fluid aver. vel.	Kinematic viscosity
	μm	μm	$\mu m/\mu s$	$\mu m^2/\mu s$
CSA1	75	50	0.05 - 1	0.79
CSA2	75	50	1	0.79 - 10
CSA3	150	50	0.05 - 1	0.79
CSA4	50 - 300	50	1	0.79

Table 5.2: Investigated geometrical and fluid parameters influencing fluid properties in cylindrical annulus with squared cross-section

In Figure 5.7, we can see results for simulations in cylindrical annulus. The general conclusion is the same as in previous case - the position of the fastest flow is shifted closer to the outer wall with increasing Dean number. The curves CSA1 and CSA2 overlays considerably - as in previous case, these curves arise from simulations with constant geometry, only the velocity and the kinematic viscosity have changed.
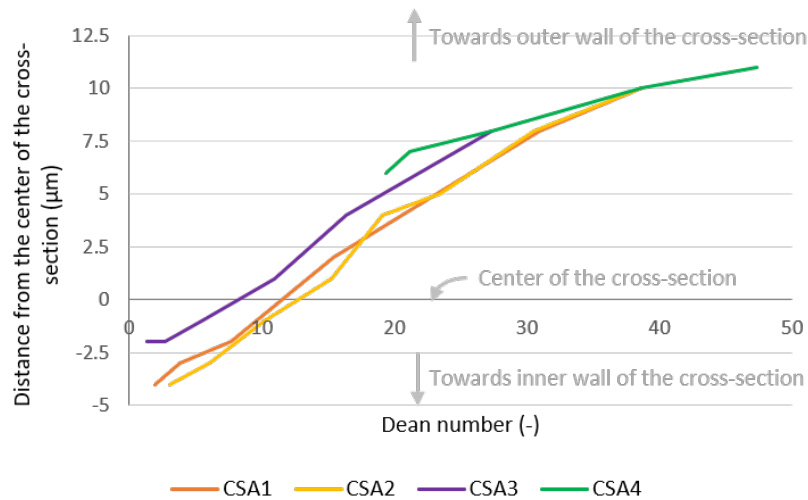
Figure 5.7: Position of the fastest fluid within a cross-section for cylindrical annulus, as a function of the Dean number. Negative values indicate deviation towards inner wall, positive values indicate deviation towards outer wall of the channel.

For the helix, the place where we examined the flow was as far from the source as possible. In all simulations, the helix had four loops. The periodic boundary conditions available in ESPResSo cause the Dirichlet fluid source to appear at the opposite side of the simulation channel as well. Therefore we examined the flow two loops from the source "above" and two loops from the source "below".

Simulation batch	Curvature radius	Section radius	Pitch	Fluid aver. vel.	Kinematic viscosity
	μm	μm	μm	$\mu m/\mu s$	$\mu m^2/\mu s$
H1	75	25	60	0.05 - 1	0.79
H2	75	25	60	1	0.79 - 5
H3	150	25	60	0.05 - 0.8	0.79
H4	75	25	60 - 450	0.8	0.79
H5	75 - 300	25	60	0.8	0.79

Table 5.3: Investigated geometrical and fluid parameters influencing fluid properties in helix

Finally, in Figure 5.8, we can see the results for simulations in helix. The curves H1 and H2 overlay in a similar way as T1 and T2 in case of torus. The curves H1 and H2 are, similarly to T1 and T2, obtained from simulation where the geometry of the channel was not modified, but we varied only parameters related to fluid.
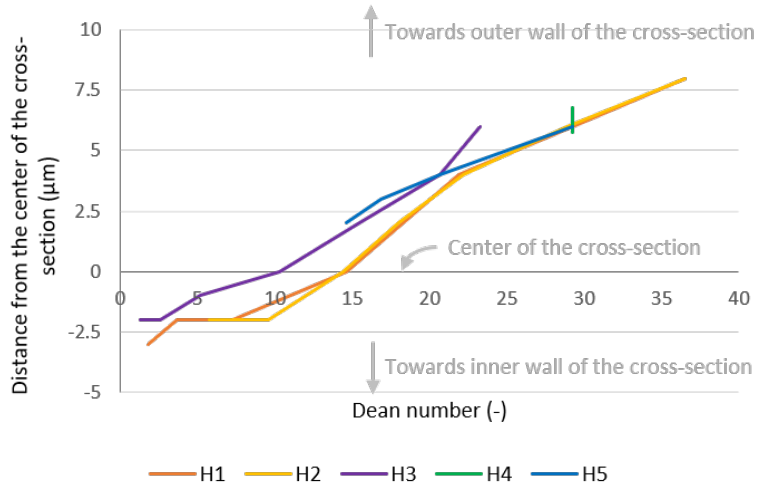
Figure 5.8: Position of the fastest fluid within a cross-section for helix, as a function of the Dean number. Negative values indicate deviation towards inner wall, positive values indicate deviation towards outer wall of the channel.

64

Dean effect in curved channels

- For a given geometry, form of the Dean vortices depending on velocity

- Speed of inertial flow in Dean vortices as a function of average speed and big radius

- Vorticity of inertial flow as a function of average speed and big radius

After the fluid flow distribution, we examined also the inertial effects in curved channels. To visualise the inertial flow, we ignored the part of the fluid velocity that was perpendicular to the examined cross-section. We kept only the part of the fluid velocity lying in the plane of the cross-section. For all of examined geometries, we studied the perpendicular cross-sections, with respect to the local axis of the channel. For the helix, we studied also a cross-section, which was parallel to the general axis of the helix.

For the perpendicular cross-sections, we could observe the Dean vortices in all of the geometries. Their form changed slightly with the average fluid velocity.

For the torus with circular cross-section, the Dean vortices from batch T1 are visualised in Figure 5.9. From the previous section we know, that the position of the fastest flow in the fluid is also dependent on the average fluid velocity. The center of the Dean vortices is moving in the same direction as the position of the fastest flow. Generally, the peak velocity is twice as big as the average velocity, which is mentioned above each case.
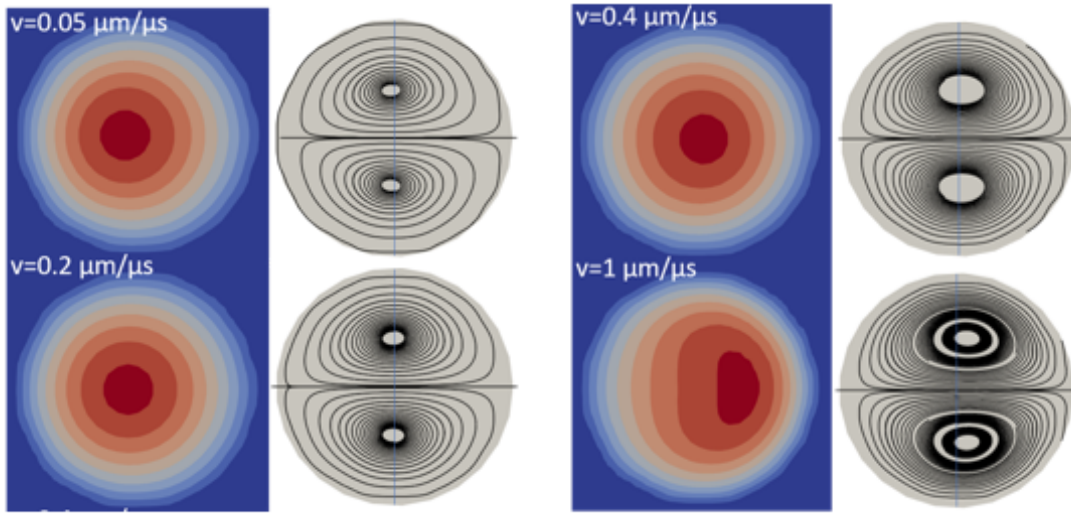
Figure 5.9: Position of the fastest fluid within a cross-section for torus, with Dean vortices. Indicated velocity is the average velocity. Images are from the computational batch T1. The blue color represents fluid with zero velocity, the red color represents the fluid with the maximum velocity.

For the cylindrical annulus with squared cross-section, the results from batch CSA1 are visualised in Figure 5.10. Figure shows the locations of the maximum flow velocity in the channel with square-section cylindrical ring geometry and the Dean vortices in the channel in the simulations of the CSA1 series (see Table 5.2 for details of the CSA1 series simulations). It can be seen from the figure that the higher the fluid flow rate, the more the position of the maximum flow rate deviates towards the outer wall of the channel. The form of the Dean vortices copy the form of the channel cross-section. Generally, the peak velocity is twice as big as the average velocity, which is mentioned above each case.

In Figure 5.11, we can see evolution of the velocity distribution over variable curvature radius Rc. When we compare the selected curvatures, we can notice in the cross-section of the channel that the position of the maximum velocity moves towards the outer wall of the channel with the smaller curvature radius Rc. In some cases, when the velocity peak was shifted very close to the outer wall, we can observe a splitting of the fastest spot into two separate locations. This effect is caused by the squared form of the cross-section, see the last illustration on the right side in Figure 5.11.
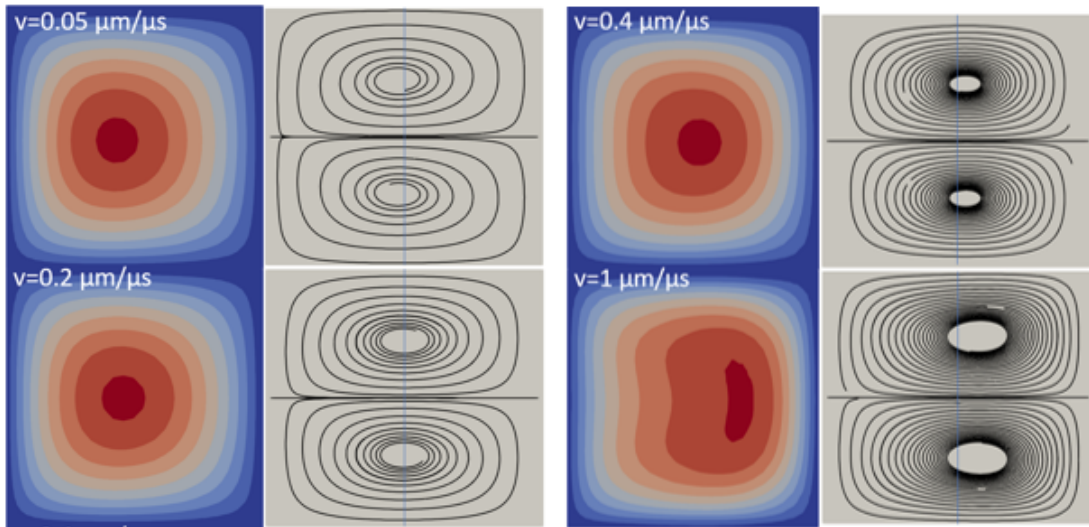
Figure 5.10: Position of the fastest fluid within a cross-section for cylindrical annulus, with Dean vortices. Indicated velocity is average velocity. Images are from batch CSA1. The blue color represents fluid with zero velocity, the red color represents the fluid with the maximum velocity.
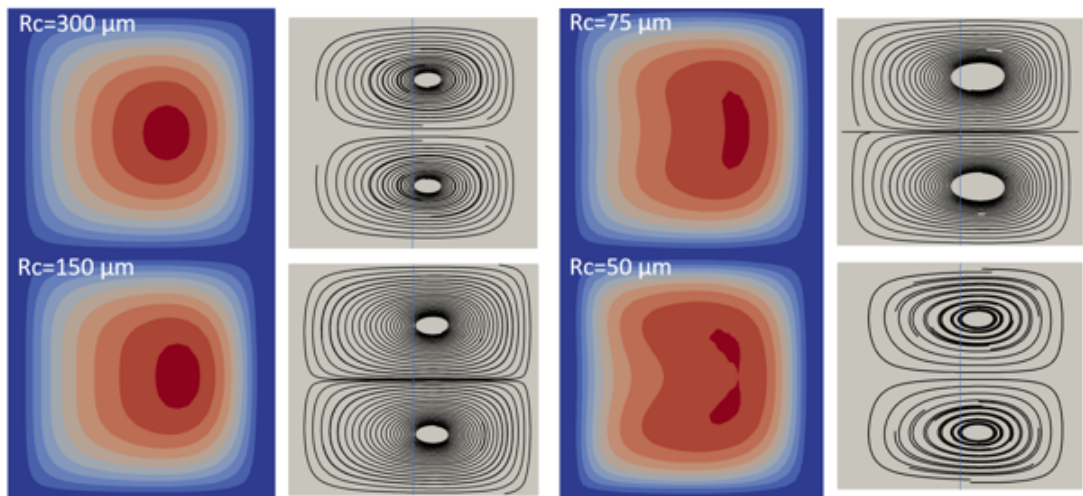
Figure 5.11: Position of the fastest fluid within a cross-section for cylindrical annulus, with Dean vortices. Images are from batch CSA4. The blue color represents fluid with zero velocity, the red color represents the fluid with the maximum velocity, which is in this case approximately $2\mu m/\mu s$.

For the helix, we could see in most of the cases an enclosed Dean vortices. We can find several exceptions for small velocities - for some geometries it could be from

5×10^{-2} to $2 \times 10^{-1} \mu m / \mu s$, where the Dean vortices were considerably deformed. In Figure 5.12, we can see evolution of the velocity distribution and the form of the streamlines with increasing average fluid velocity, for batch H1. In Figure 5.12 we can see also the S-shaped streamlines. The curvature of these streamlines is more pronounced for higher average fluid velocities. Generally, the peak velocity is twice as big as the average velocity, which is mentioned above each case.
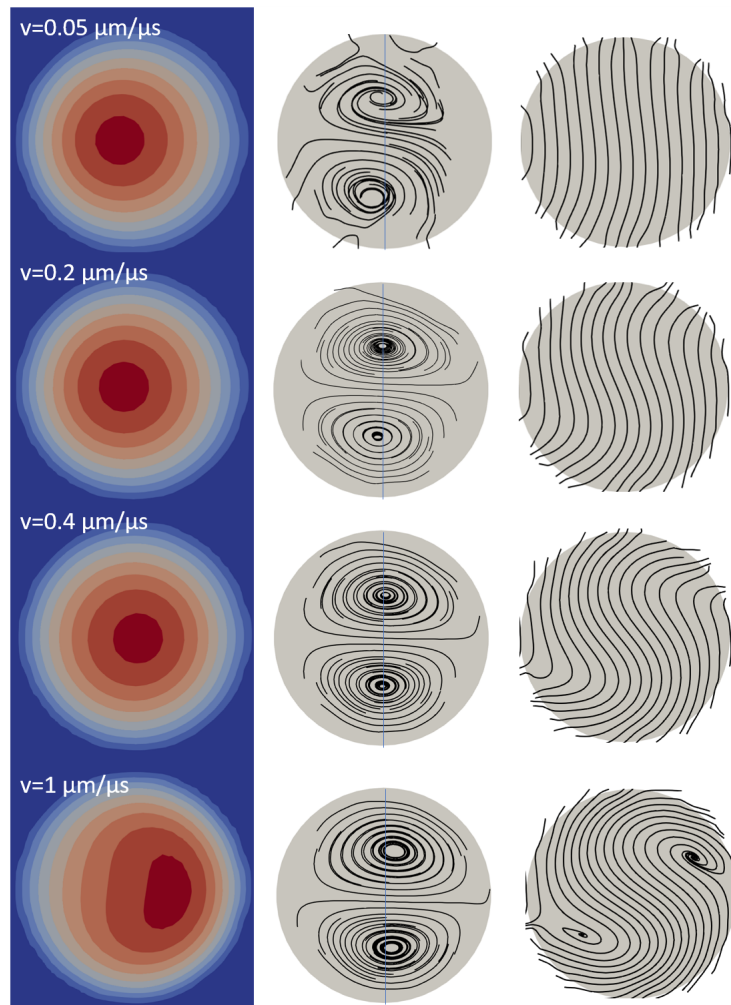
Figure 5.12: Position of the fastest fluid within a helix, shape of the Dean vortices, and S-shaped streamlines. The position of individual formations depends on average fluid flow velocity, for batch H1. Indicated velocity is average velocity. The blue color represents fluid with zero velocity, the red color represents the fluid with the maximum velocity.

The curve H4 show us dependence of the fastest flow position on the helix pitch. The values of examined pitch varied between 60 and 450 μm. The angle of the perpendicular cross-section, with respect to the ax of the helix, varied from 7° to 44°. Despite of this rather significant variation, the distance of the fastest flow did not change considerably. The difference could be seen in position of the fastest flow - it was not positioned on the straight line between the inner and the outer wall, but with the bigger pitch, the position of the peak was more tilted from this line, Figure 5.13.
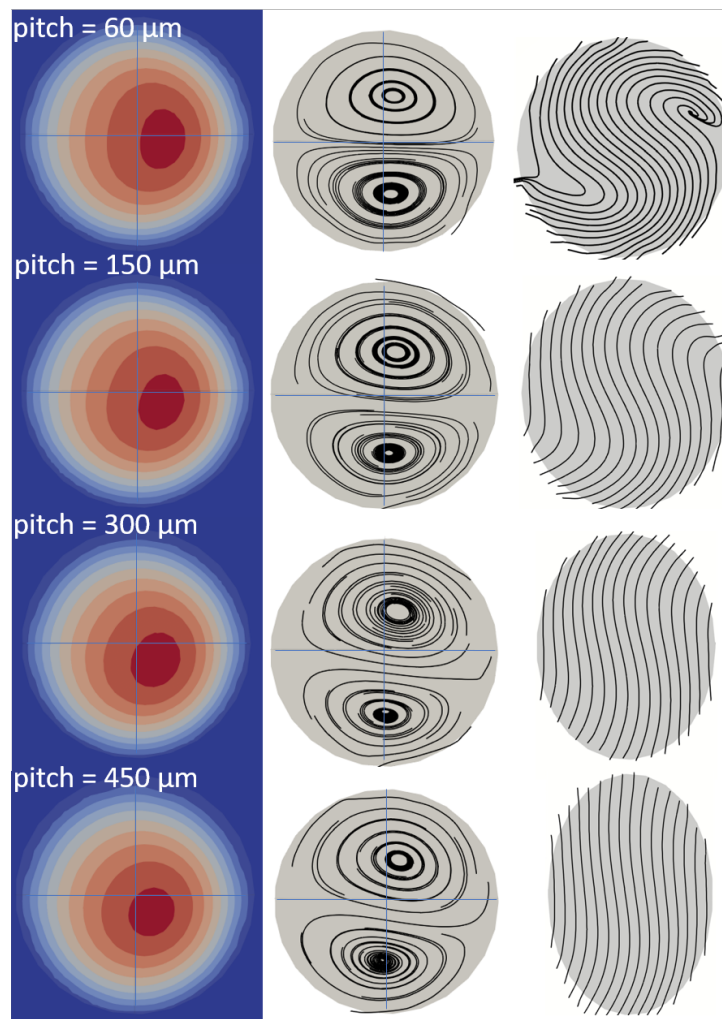
Figure 5.13: Position of the fastest fluid within a cross-section for helix, Dean vortices and S-shaped streamlines for batch H4 with variable pitch. The blue color represents fluid with zero velocity, the red color represents the fluid with the maximum velocity, which was in this case app. $1.6\mu m/\mu s$.

We examined also the relation between the speed of the inertial flow and the average velocity of the fluid in channel. We used batches H1 and H3 to examine the relationship. For each simulation, we identified the velocity of the inertial flow in Dean vortices, and compared it with average fluid velocity in channel. This relation appears not to be linear, as we can see in Figure 5.14. For batch H1, and for the slowest flow with average velocity of $5 \times 10^{-2} \mu m/\mu s$, the velocity of the inertial flow was only of $1.5 \times 10^{-3} \mu m/\mu s$, which is 3% of the average fluid velocity. For the average velocity of $8 \times 10^{-1} \mu m/\mu s$, the inertial velocity was about $2.7 \times 10^{-1} \mu m/\mu s$, which is 33% of the original value.
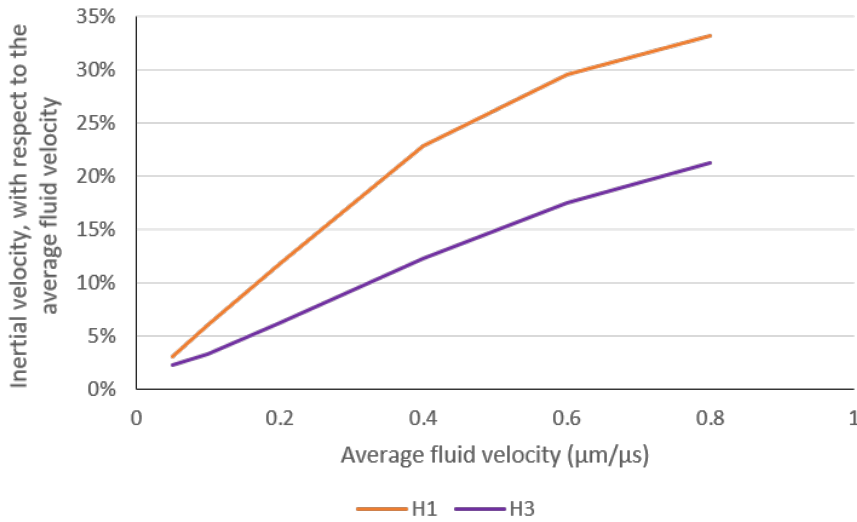
Figure 5.14: Dependence of the inertial velocity on the average fluid velocity.

The intensity of the inertial flow can be described also by vorticity. This parameter was examined also in batch H1 and H3, and the evolution of the vorticity is presented in Figure 5.15. The most important vorticity can be seen in a geometry with smaller curvature radius and for the high values of average flow velocities.
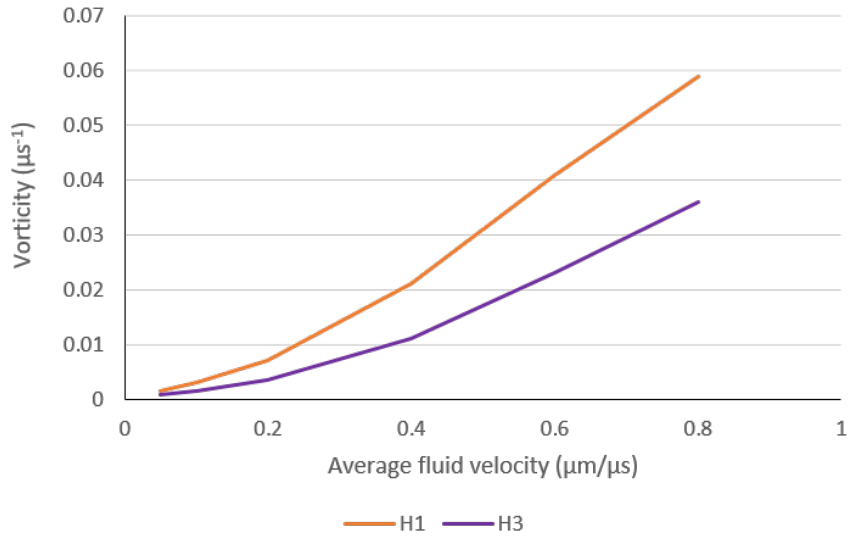
Figure 5.15: Dependence of the vorticity of inertial flow on the average fluid velocity.

5.4 Conclusion

In this analyses of Dean effect, we examined inertial flow in curved channels. We identified Dean vortices in all geometries.

We showed an interesting phenomenon: Despite the centrifugal force that would normally shift the fast flow towards the outer wall, we showed that for the low Dean numbers, this shift is towards the inner wall. This effect is clearly visible in Figures 5.6-5.8. The explanation for this phenomenon was given in [36]. The surface area of the inner wall is smaller than the outer wall, and thus the fluid experiences less friction force from the inner wall than from the outer wall. With low R_e, the viscous force (friction force) dominates the flow because of weak inertial effect, giving rise to a higher flow velocity near the inner wall. As R_e increases beyond a critical value, inertial effects dominate the flow, and thus the flow near the outer wall is stronger that near the inner wall.

The exact form of the Dean vortices and of velocity distribution is, in a channel with fixed geometry, dependent only on Dean number, in other words on the ratio of velocity of the fluid and its kinematic viscosity. When the geometry of the channel changes, the Dean number is no more the only parameter that influences the velocity distribution in the channel.

Finally, we examined influence of the coil pitch in helical simulation channels. This parameter, surprisingly, do not seem to have significant influence on the velocity distribution within the perpendicular cross-section, in the analyzed range of the pitch values.

The next step in our research is to examine the behavior of cells flowing through curved microfluidic channels. In direct channels with a regular cross-section, the neutrally buoyant particles are influenced by a drag force induced mainly by the principal flow in direction of the channel. The drag force, which acts in direction of the fluid flow velocity, will have different character in curved channels. The drag force will be partly deviated by inertial flow, that will have an important impact to trajectory of those particles mainly in channels with fast flow. The question that we would like to answer is what influences the trajectories of the particles of flow, whether there could find a stabilised trajectories, or rather a "patterns" in trajectories, for example an additional spin around the stabilised trajectory, caused by Dean vortices.

This results have three important consequences:

- Dean vortices are present in all examined curved geometries, we can continue to make studies of their sorting capacity

- Helix pitch does not influence very much the fluid flow distribution within the cross-section

- for a given geometry, we can use only the Dean number to determine the position of the fastest fluid flow

6 Particle separation

The aim of the work is to make a proposal of a spiral microchannel for a Dean's flow verification and we have prooved this secondary flow in Chapter 5 in several types of the cross-sections in curved channels. But as the second aim of this work is to separate particles, we still did not have results like we know from the theoretical literature. We were not able to separate particles. They still focus near the outher wall. We need to design more suitable microchannel and also try to change the properties of the flow and particles. In order to get better results, we realized to change the microchannel at all.

Our interest in the following chapter was to find out whether the size of the particles in the channel flow influences particle focused positions and if it is possible to separate them. In addition to the size of the particles, we also investigated the effect of the fluid velocity on the fixed positions of the embedded particles.

The most of this chapter was publicated in a paper [3] as a part of conference paper.

6.1 Computational study

We have chosen square serpentine channel (c_1) from the 1.2 for this computational study. One could ask, why this one was chosen, but the answer to that question is that while there were problems in 4.2, where we tried spiral square serpentine channel, the limitations of the ESPResSo package did not allow us to continue. In the article [37], the authors analyze focusing positions of the $5\mu m$ and $10\mu m$ particles in the three curved channels for various channel Reynolds numbers. They analyze zigzag channel, which has not been used previously for inertial focusing studies, in comparison with a serpentine channel and a square wave channel. Based on this article we decided to try square serpentine channel to compare $5\mu m$ and $10\mu m$ particles in the flow.

6.1.1 Numerical model

We use well-established computational model of fluid and the immersed particles or cells. Here, the liquid is calculated with the lattice-Boltzmann (LB) method [1]. The cells are taken into account as immersed objects with fully 3D discretization using tetrahedrons that cover whole inner space inside the sphere. At the edges of the small tetrahedrons, fairly rigid springs are set so that the object almost does not undergo any deformation during the flow. Detailed description of the underlying models are available in [18, 19, 2]. The validation and verification of the computational models has been provided in [16, 15, 32]. For all simulations we used tetrahedral meshes with edges of sizes approximately 0.4 μm.

6.1.2 Final geometry for particle separation

Our aim is to simulate rectangular serpentine channels as depicted in Figure 1.2 (c_1). In the figure, there are only six S-shaped repeating sections displayed, however in practise, there are more sections needed to obtain desired focusing positions. Together with long straight channels before and after serpentines, the whole channel is too large to model at whole. Therefore we will model only one repeating section (between the dashed seeding and reseeding line in Figure 6.1) enlarged by fluid evolution sections before and after, with periodical boundary conditions at the inflow and outflow. This way we ensure that the fluid is fully evolved at the seeding and reseeding lines. Periodicity of the middle section allows to reseed the cells back to the seeding line as soon as they reach the reseeding line. Their relative position at the cross-section is preserved during the reseeding, as well as their velocity.

After initial seeding of particles on the seeding line in the channel at the beginning of the flow, we watched the positions of the origins of the particles during the flow. When the particles have arrived to the reseeding line, we reseeded them back to the seeding line with the new coordinates of the particle origins and we have continued the watching of these origins coordinates. With this kind of reseeding by repeating the S-shaped section, as you can see on the picture in Figure 6.1, we have done a simulation of periodical flow without real construction of the real microchannel. As a result we get the trajectories (from the origin coordinates during the flow process). In Section 6.2 you can see analyses.

74
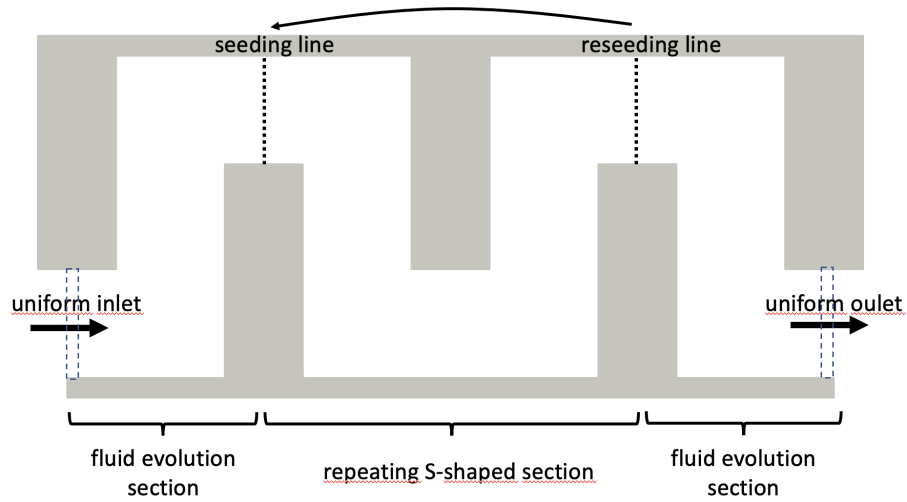
Figure 6.1: Simulation box for the case of the cross-section with dimensions $80 \times 40\mu m$. One repeating S-shaped sections enlarged by two fluid evolution sections.

Since we study three different cross-sections, the respective dimensions of the channels are different for all three cases. The respective dimensions of channels are depicted in Figure 6.2. Note that the lengths of the channel along the axial center of the channel are preserved.
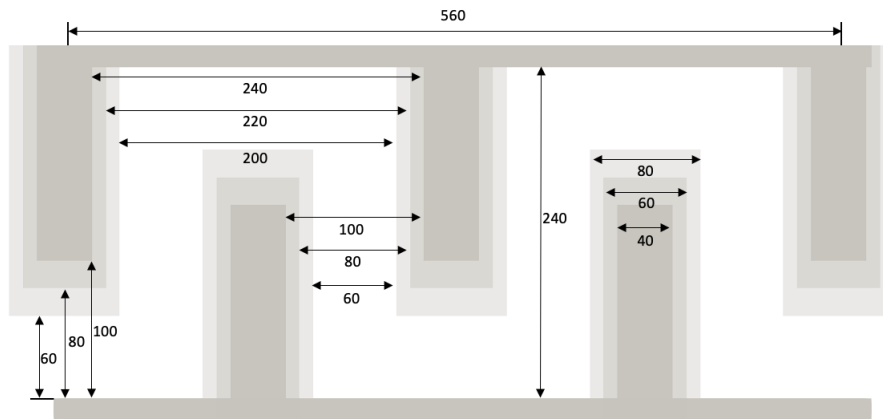
Figure 6.2: Dimensions of three different geometries in μm. The darkest boundaries represent $100 \times 32\mu m$, the medium dark represent $80 \times 40\mu m$ and the brightest represent $60 \times 52\mu m$ cross-section.

6.1.3   Geometry and fluid set-up

To create a specific geometry as a serpentine channel, we need to define boundaries in the simulation box. This is done using geometrical shapes of rhomboids in the open-source scientific simulation package ESPResSo with PyOIF module [18]. To let the static fluid at the beginning of the simulation fully evolve, we simulate $500\mu s$ without the particles. The uniform boundary conditions at inlet and outlet define the average velocity in the channel which is proportional to the volumetric flow rate. This can be done in PyOIF using a special velocity boundary (visualized in Figure 6.1 by dashed rectangles), with predefined constant values of velocity field at the boundary points.

Specific values of the inlet conditions and the corresponding flow rates are presented in Table 6.1.

Average velocity $[\mu m/\mu s]$	Reynolds number $[-]$	Volumetric flow $[mL/min]$
0.18	19.2	0.035
0.35	37.3	0.062
0.45	48	0.086
0.6	64	0.115

Table 6.1: Fluid parameters in $80 \times 40\mu m$ rectangular channel. Values in channels with other cross-sections are similar.

We are interested in studying the flows in physically relevant cases. We consider fluid with density and viscosity similar to physiological solutions or water being $1000kg/m^3$ and $10^{-3}Pa.s$. In inertial microfluidics, the relevant ranges for the Reynolds number are up to 100 [37]. We consider four different average velocities up to $0.6m/s$ in the channel so that Reynolds number varies up to 64. For maximal velocity for evaluation of Reynolds number in (3.5) we take the double of the average velocity. With cross-sectional area of around $3100\mu m^2$ it accounts for the volumetric flow rate being up to $0.115mL/min$.

6.1.4   Particle seeding

For simulations in chosen geometry, we firstly seeded 58 particles deterministically. We devided them with the same space of $7\mu m$ along to y-axis and also with the same space of $7\mu m$ along to z-axis. We observed a problem with particles near the middle of the channel. Those particles did not behave as we expected. They did not focus after some flowing to the inner or outer wall. This was the reason to change particle seeding. Based on the article [13], where the particles are focused in two stable positions in straight channels with a rectangular cross-section, we started to place our particles randomly, but in close neighbourhood of the two concrete positions, see Figure 3.1, (d). This kind of distribution ensures that no particles will be exactly in the middle of the channel. We wanted the placement randomly, so we used the normal distribution for seeding particles around this two positions.

As you can see in Figure 6.3, we have three different geometries that differ in the cross-section of the channel with particles (depicted by blue dots). We seeded them at the beginning of every simulation by normal distribution with same standard deviation, which we chose around these two positions (depicted by red dots). In order to assure the reproducibility of the experiments we used the same random seeding for $5\mu m$ particles and $10\mu m$ particles. We also used the same random seeding for every fluid velocity in simulations.
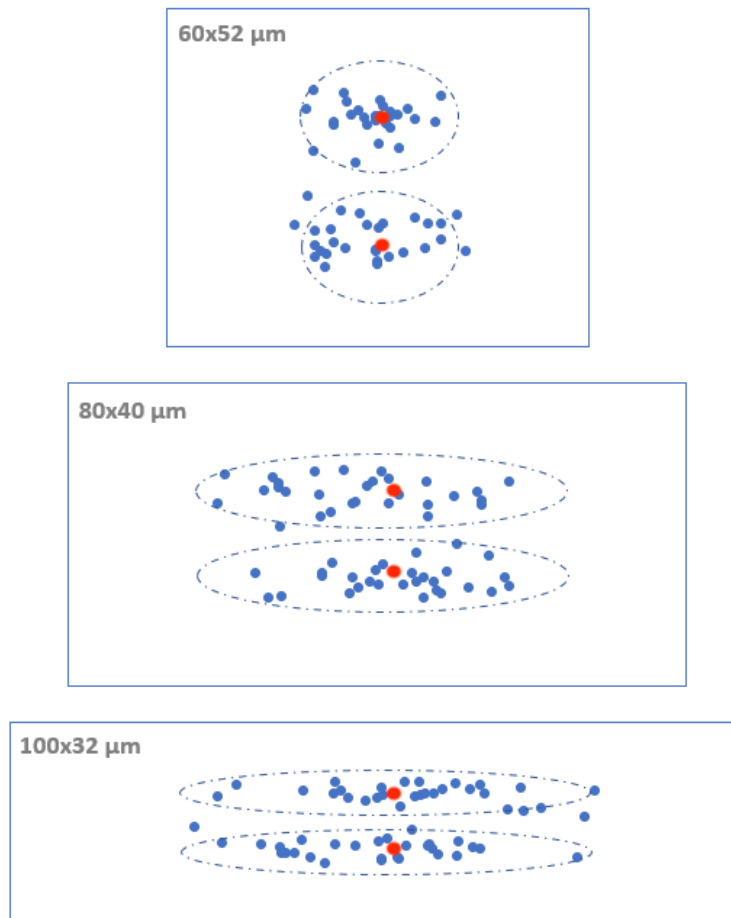
Figure 6.3: Three different cross-sections of rectangular channels with particle seeding. Centers of the particles (blue dots) are depicted distributed by normal distribution around stable positions of straight channels (red dots).

In the Figure 6.4 you can see final part of rectangular serpentine microchannel created in ESPResSo package and visualized in paraview. The simulation box consists of geometrical shapes of rhomboids like boundaries, fluid flowing around them and particles immersed. Lines represent particle trajectories based on fluid velocity. Higher fluid velocity has red lines, lowest has blue coloring.
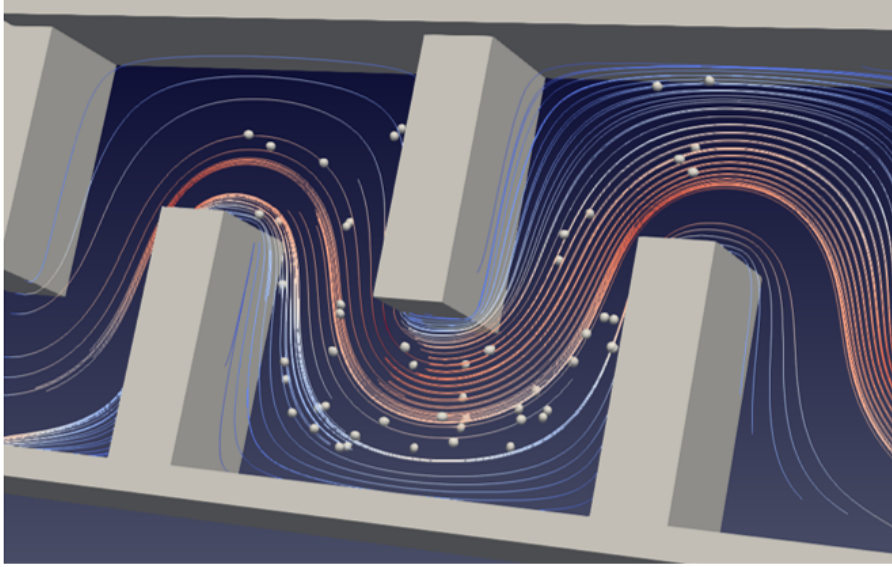
Figure 6.4: Final channel with particles immersed. The lines represent particle trajectories.

6.2 Computational results

Our aim is to examine how the stable positions within several cross-sections are dependent on geometric parameters of the channel. We compared three different cross-sections in square wave channel and in each cross-section, we modified average fluid velocity and the size of the particles. The other parameters were kept constant. In Table 6.2 we present values of the parameters that were examined. Together we run 24 simulations.

Particle size	Average velocity	Cross-section
μm	$\mu m/\mu s$	$\mu m \times \mu m$
5	0.18	60×52
10	0.35	80×40
	0.45	100×32
	0.6	

Table 6.2: Overview of three varying parameters: size, velocity and cross-section. Simulations have been performed for all 24 combinations.

6.2.1 Focusing length

First we need to determine the focusing length of the channel. We tracked the trajectories of the cells until the particles reach stable region. Each of the 24 simulations was run such that at least 28 passes of the particles through the repeating S-shaped section occurred.

In Figure 6.5 we see four $100 \times 32\mu m$ cases: 5 and $10\mu m$ particles each for two different Reynolds numbers. Horizontal axis shows the number of passes through the repeating S-shaped section and vertical axis shows the particle position along the width of the channel ranging from 0 to $100\mu m$ in these cases. We can clearly see when the particles start stabilize and we can define the minimal focusing length. In the figure we show trajectories for only two values of Reynolds number, however, taking account of all four values we arrive at the focusing length for cross-section $100 \times 32\mu m$ to be 19 passes. Analogous we deduce 15 passes and 18 passes to be focusing lengths for $60 \times 52\mu m$ and $80 \times 40\mu m$, respectively.

After determining the focusing length, we further work with positions of particles across the channel width at the moment of passing this focusing length.
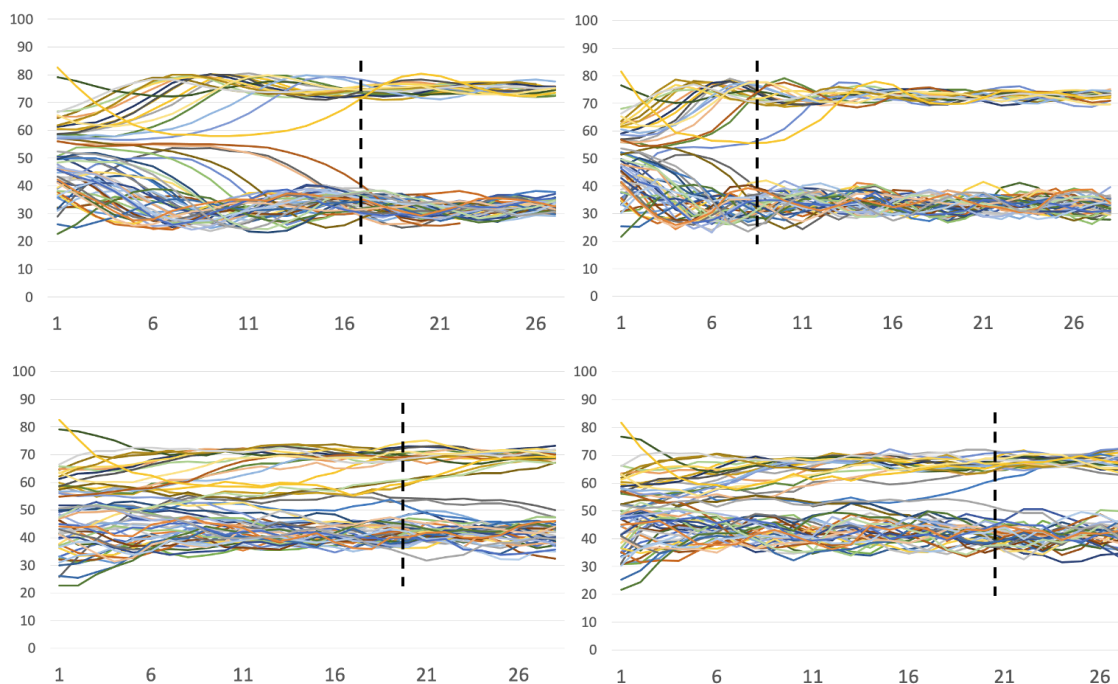
Figure 6.5: Trajectories of $5\mu m$ particles (top figures) and $10\mu m$ particles (bottom figures) in channel with $100 \times 32\mu m$ cross-section for Reynolds number 37.3 (figures on the left) and 64 (figures on the right). Black vertical lines indicate minimal focusing length. Horizontal axis gives number of passes through the repeating S-shaped section. Vertical axis gives particle position across the width of the channel.

6.2.2 Particle separation

The three different geometries achieve different focusing performance for small and large particles. All three geometries have different focusing length but this is not a limitation: Once we pick the desired geometry, the channel length will be adapted accordingly. The particle focusing positions are either distinct and separated to more positions or focused along the center of the channel width. In some cases we could separate them, but in some cases they are fully overlapping. The results are depicted in Figures 6.6 – 6.8.

For the case of 60×52 rectangular channel we assigned the smallest focusing length. The particles were focused already after 15 times of S-shaped sections repeating. However we get almost fully overlapping distributions of $5\mu m$ and $10\mu m$ particles across the channel width.
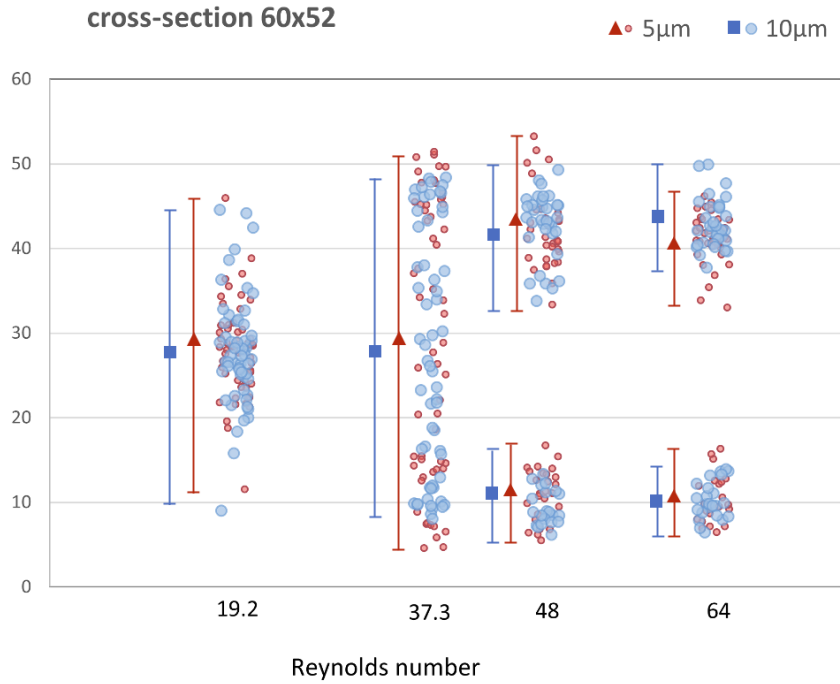
Figure 6.6: Particle focusing in $60 \times 52\mu m$ cross-section for various Reynolds numbers. Focusing length was 15 passes of the repeating S-shaped section. Vertical axis gives particle position in $[\mu m]$ across the width of the channel.

In 80×40 rectangular channel we can stop the simulations after 18 passes of S-shaped section. We can observe the best focusing performance for the Reynolds number between 32 and 50. The $5\mu m$ particles are separated in two positions across the channel width. The $10\mu m$ particles are focused along the center of the channel width, and the width of particle distribution gradually decreases to a single stable focusing line with higher Reynolds number. At Reynolds numbers 37.3 and 48 we can see in Figure 6.7 slightly overlapping of focusing sections for $5\mu m$ and $10\mu m$ particles which may result in non-perfect separation. This contributes to the best possibility of separating particles of two sizes. For the highest Reynolds number we can see overlapping of these two different particle sizes and it is not able to separate them.
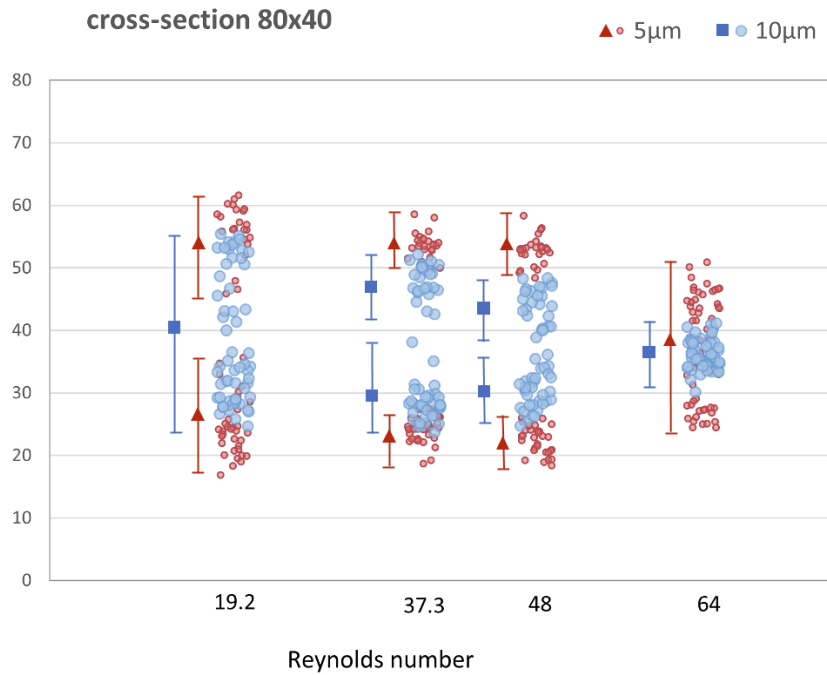
Figure 6.7: Particle focusing in $80 \times 40 \mu m$ cross-section for various Reynolds numbers. Focusing length was 18 passes of the repeating S-shaped section. Vertical axis gives particle position in $[\mu m]$ across the width of the channel.

For the case of 100×32 rectangular channel we needed 19 passes of the S-shaped section to get the best focusing of the particles. The $5 \mu m$ particles have the best particle separation possibility. The focusing positions are fully distinct and we get the biggest gap between them as you can see in Figure 6.8, more than $30 \mu m$ with Reynolds numbers 37,3 and 48. In this case, we have larger range of Reynolds numbers for separation.
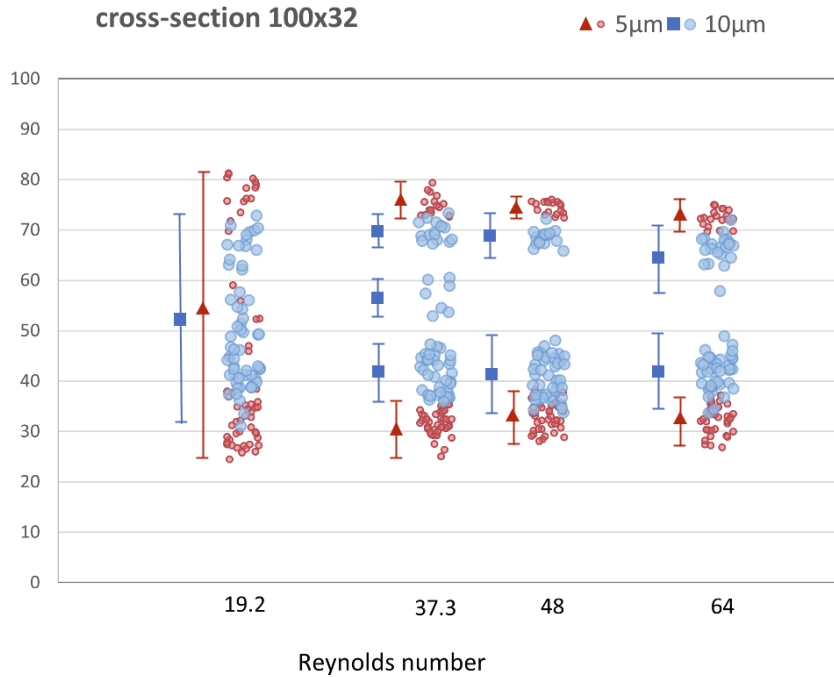
Figure 6.8: Particle focusing in $100 \times 32 \mu m$ cross-section for various Reynolds number. Focusing length was 19 passes of the repeating S-shaped section. Vertical axis gives particle position in $[\mu m]$ across the width of the channel.

6.3 Conclusion

To compare various cross-sections, we can draw several conclusions.

First observation is that the $60 \times 52 \mu m$ cross-section is not suitable for particle separation. Although the particles focused after the shortest distance, the focused position of particles overlap for both analyzed sizes.

As previous results from [37] suggested, a good candidate for separation is the channel with $80 \times 40 \mu m$ cross-section. This was confirmed by our computations and indeed, with Reynolds numbers 37 and 48 we get the possibility for particle separation. In this cross-section, with higher Reynolds numbers we loose the possibility for separation because particles of both sizes drift towards the center of the channel. $10 \mu m$ particles focus in narrower strip (width $10 \mu m$) while $5 \mu m$ particles focus in wider strip (width $30 \mu m$). However, the two strips completely overlap.

The results for cross-section $100 \times 32\mu m$ give larger possibility for separation. Not only the offer separation for Reynolds numbers 37 and 48 but also at 64 we still have distinctive focusing position for particles of different sizes. Again, with increasing flow velocity we see tendency of particles to focus closer to the channel center, however this tendency is much weaker than for $80 \times 40\mu m$ cross-section and the particles still leave a particle-free strip in the middle of the channel. This results have two important consequences:

- Higher throughput is possible due to large Reynolds number and thus larger fluid velocity.

- Separation of even large particles is possible. Since $5\mu m$ and $10\mu m$ particles leave a particle-free strip in the middle of the channel, it may be possible to separate a third size of particles that would focus right in that strip.

6.4 Results verification

We present experimental results that are in a good agreement with our computational simulations.

An interesting result from Figure 6.9 is that the arrangement of particles of different sizes varies across the channel width. In order to intuitively show the distribution of particles, they graphically show the focusing positions and their deviations for two particle sizes. These particle focusing positions are either distinct and can be separated, or they are overlapping and they cannot be separated. For lower Reynolds numbers 12.5 - 37.5, smaller particles partially overlap with larger particles, so we are not able to separate the particles according to their size. At Reynolds number of 50 - 75, the figure shows that the smaller particles in the channel cross-section cluster on the two sides away from the large particles and the larger particles stabilize along the center of the channel. This creates the possibility of separating particles of two sizes. For Reynolds number higher than 75, particles are overlapping, so the separation is not possible. The optimal separation performance appears in this square wave channel at Reynolds number 50 and 62.5.
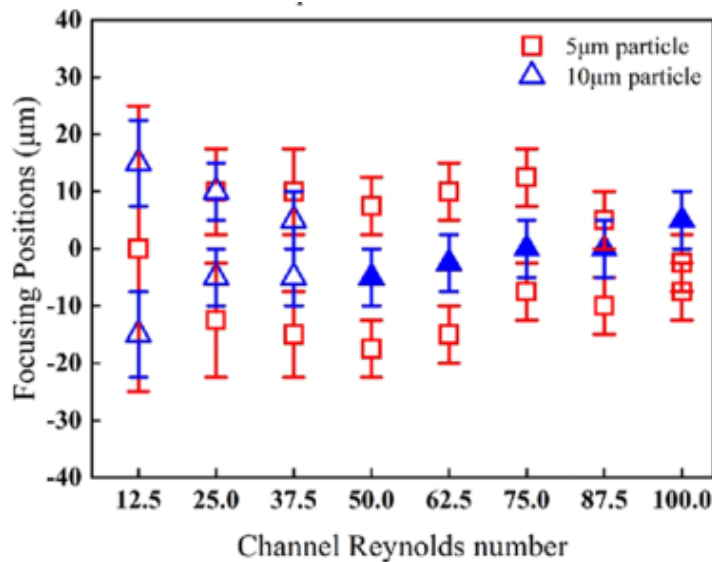
Figure 6.9: Focusing positions of $5\mu m$ particles (red coloured) and $10\mu m$ particles (blue coloured) in channel cross-section in square wave channel. Reprinted from [37].

In comparison with our results, from S-shaped channel for the cross-section of $80 \times 40 \mu m$, that represents our best result, we can see similarity depicted in Figure 6.10. For all Reynolds numbers particle focusing positions are not completely distinct and we can see there slightly overlapping parts. But smaller particles are focusing on two locations and larger ones to the middle of the channel width. For the smallest Reynolds number and for the highest one, we are not able to separate particles according to their size. They are almost fully overlapped. But for Reynolds number 37.3 and 48 we get possibility for particle separation, despite the fact that separated samples would not be 100% clean.

To conclude, we have very good agreement with results presented in [37] for the square wave channel with cross-section $80 \times 40 \mu m$. This validates our computational approach.
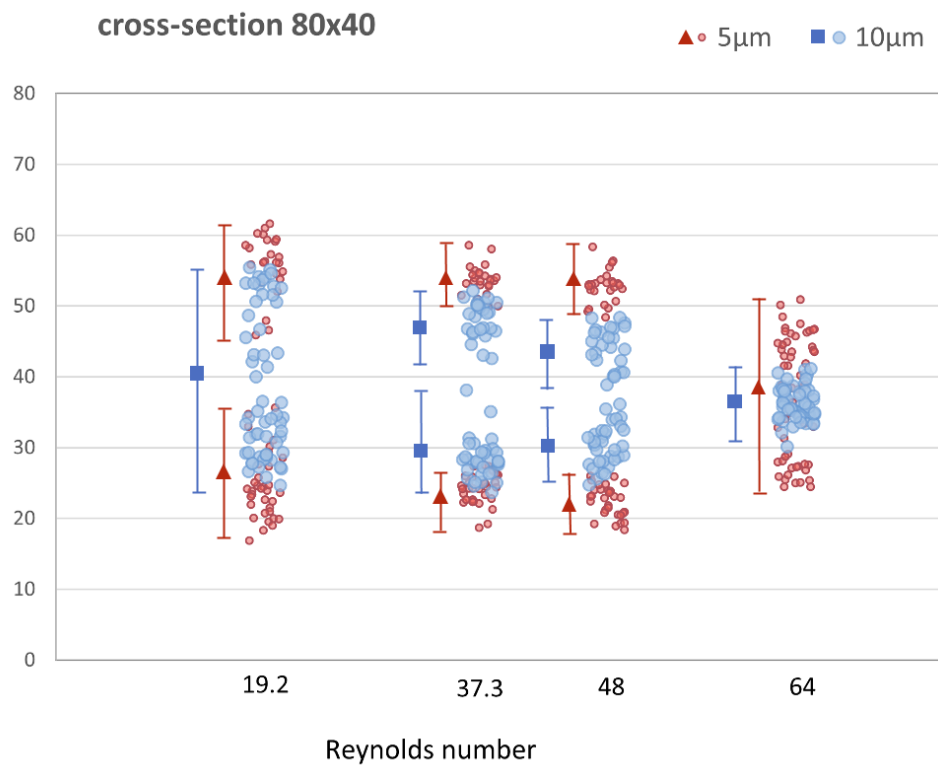
Figure 6.10: Focusing positions of $5 \mu m$ particles (red coloured) and $10 \mu m$ particles (blue coloured) in channel cross-section from square serpentine channel.

A similar experimental study was performed in [38]. The authors focus on high throughput extraction of plasma using a secondary flow-aided inertial microfluidic device. They report the development of a simple inertial microfluidic device with a serpentine channel for efficiently separating blood cells from plasma. The working mechanism of this device relies on the two-sided secondary flow aided inertial focusing of particles in a serpentine channel. Specifically, blood cells were focused along two sides of the channel, while the blood plasma was collected at the cell-free region within the channel center. The device was tested with diluted whole blood. The authors fabricated device with eight parallel serpentine channels. The blood sample was taken from a healthy adult male volunteer, and it was contained within a vacutainer tube containing anticoagulant agent lithium heparin [38]. The blood sample was diluted before pumped into the microfluidic device. This device could be easily integrated with other sample preparation processes or detection units to form a sample-to-answer lab-on-a-chip system.
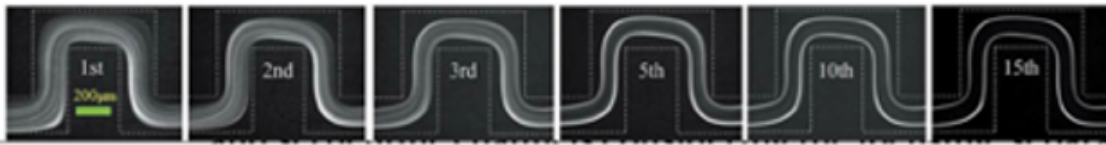
Figure 6.11: Focusing of $5\mu m$ particles in two stable positions in channel cross-section after 15 passes of S-shaped section in periodical S-shaped channel. Reprinted from [38].

As a result in Figure 6.11, at the end of the simulation, after fifteen periods, we can see two focusing positions of $5\mu m$ particles across the channel width. Figure shows also the fluorescent trajectory of $10\mu m$ particles under different periods within a serpentine channel. Fluorescent light near channel walls disappear promptly after about three periods, while fluorescent light within channel central area weakens gradually and vanishes after more than ten periods [38]. This indicates that the particles near two-sided walls migrate much faster to the equilibrium positions than their counter parts near the channel centre [38]. The cross-section dimensions of serpentine channel was set to $200 \times 42\mu m$.

To coclude, we have very good agreement with results presented in [38] for the serpentine channel. This also validates our computational approach.

7 Roughness in channels

The channel roughness also has some effect on the position of the maximum fluid flow velocity in the cross-section as well as on the stable positions of the particles in the curved channels. We would like to get some insight on the effect of roughened channel walls on the fixed particle positions in the flow of a curved channel and on the Dean flow. Adding roughness to the channel geometry is not trivial. Before particle seeding, we have to analyze the fluid flow in the channel without and with roughness. We need to compare Dean's vertices in the channels for the purpose how should we design it.

In this chapter, we describe our first draft of the roughness elements design added to our existing square serpentine channel with cross-section dimensions $60 \times 52 \mu m$ and first analyses.

7.1 Purpose of roughness

Producing of microchannels with smooth surfaces without any roughness is impossible in reality, due to the small channel dimensions. Many researches study surface roughness and their effects on microchannel possibilities. But there are two ways how to add the roughness to the channel. It can be done randomly, because manufacturing of the real microchips is not 100 % exact and surface roughness has no regular shape. The size of irregularities in this case however is up to hundreds of nanometers. The second approach is to add the roughness to the microchannel by obstacles that have dimensions significant with respect to the size of the channel, so the size of the obstacles are given in tens of micrometers.

In the article [23] about effects of surface roughness in microchannel with passive heat transfer enhancement structures we can find their approach to the production of roughing walls. They present there the effects of surface roughness, which is unavoidable due to manufacturing tolerance. They introduce the surface roughness by meshing a smooth channel. Their results show that roughness could increase the overall flow resistance.

In the next paper [28] the authors discuss roughness components with the spherical shape on the 10 million Argon atoms flowing inside the microchannel. They concluded that the spherical shape of roughness elements brings no destructive effect on the flow behavior in some concrete range of external driving force. Their study was analysed inside a cubic microchannel with ideal and roughened surfaces based on a comparison.

In research paper [11], we can see a design and metodology of two-dimensional fluid flow in the rough microchannels. The paper aims to investigate the changes in friction and pressure drop in the microchannels by considering the different roughness elements on microchannel wall and changes in elementary geometry and flow conditions. Results show a significant effect of roughness on the pressure drop and friction. They used several types of roughness elements: rectangular, trapezoidal, elliptical, triangular and complex as you can see in Figure 7.1. For their analyses needs they used the height of roughness elements from 1.25 μm to 7.5 μm. The distance of roughness elements was considered from 10 μm to 80 μm and the size of roughness elements was from 5 μm to 10 μm.
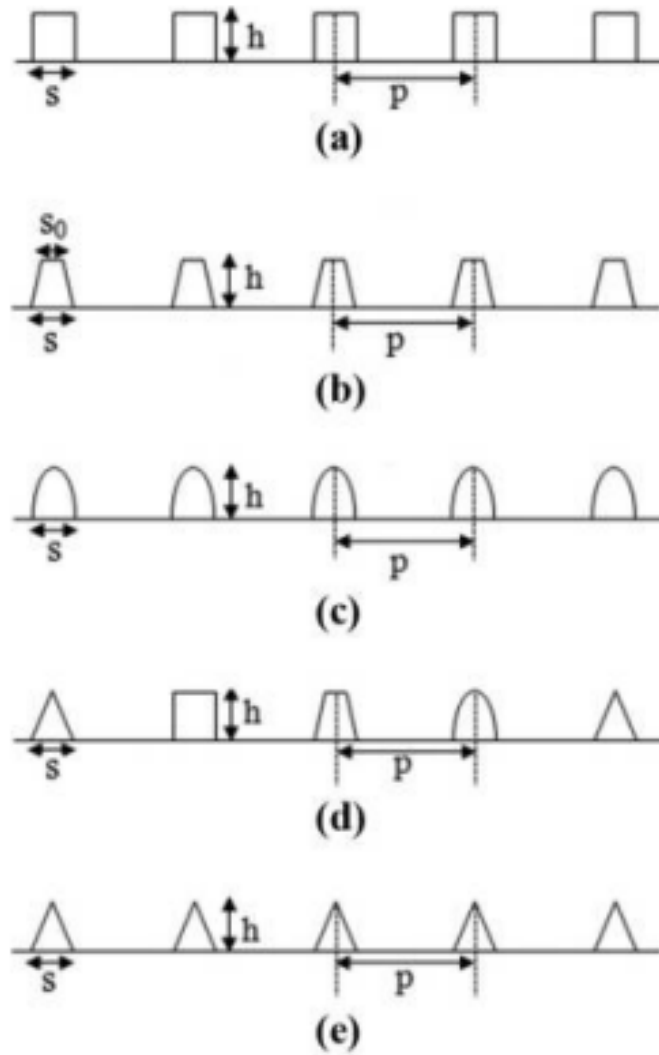
Figure 7.1: Typical roughness elements used in microfluidics: (a) rectangular triangular (b) trapezoidal (c) elliptical (d) complex and (e) triangular. Elements represent obstacles in channel walls. Reprinted from [11]. The height of roughness elements is representing by h, p represents the distance between the adjacent peaks, S represents the size of roughness and So is the width of roughness elements at the top in case of trapezoidal elements.

In our geometries in microchannels analysed for Dean's effect purpose and for particle focusing or separation, we always use flat walls in channel up to now. In a study about passive label-free microfluidic systems for biological micro-object separation, we can see a double-sided herringbone microstructures in microfluidic chip used for capture tumor cells [30], see Figure 7.2. They use hydrophoresis as a groove-based separation method. Geometric parameters of grooves, such as the width of the channel and the aspect ratio of grooves, have been investigated, proving that an increase in the channel width helps the transformation from separation mode to focusing mode. Other groove geometry innovations, such as V-shaped herringbone grooves, have been shown to be effective in cell focusing. Hydrophoresis can also be combined with labeled microfluidics to enhance the particle separation performance. The herringbone structure is always used in micromixers [30].
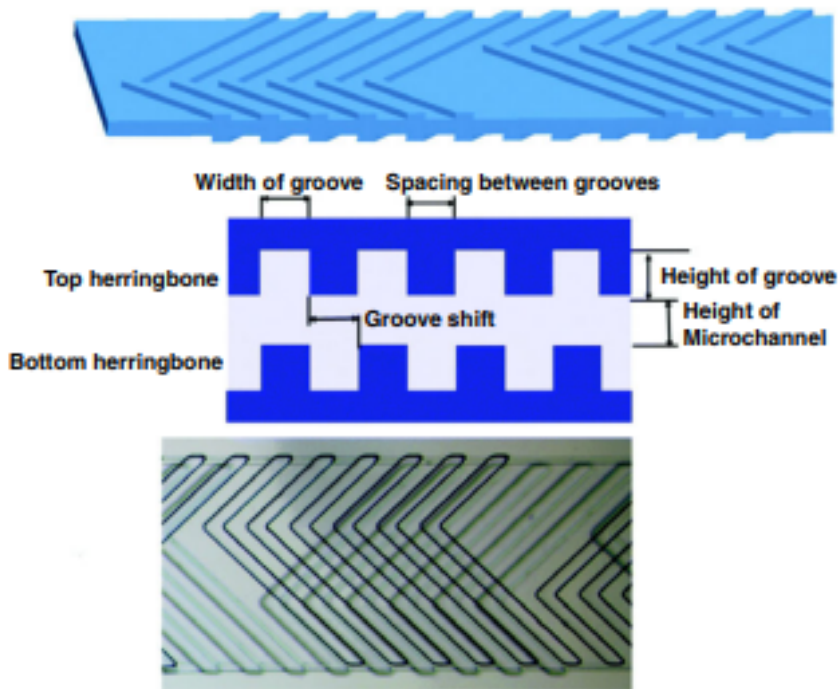
Figure 7.2: Microfluidic chip with double-sided herringbone microstructures to capture rare tumor cells, reprented from [30].

7.2 Bottom and top walls modification set up

We started with a proposal of roughness in channel geometry used in previous Chapter 6.1.2. Dimensions of the geometry used for this study and for the simulations were $60 \times 52 \mu m$. We defined a roughness elements like rectangular obstacles on the sides of the channel geometry. We were inspired by the article about roughness in microfluidic chip with double-sided herringbone from Figure 7.2, so we designed it in similar way like boundaries which the herringbone should imitate.

Because the Dean's vortices in squared cross-sections copy the cross-section of the channel, see 5.4 in Chapter 5, where we analysed the Dean effect in the fluid flow without particles to see an impact of the roughned walls. Before exact roughness boundaries definition, we need to know Dean's vortices and their direction in the new geometry cross-section.

To compare the Dean effect from the channel without any roughness with the same channel with roughness, we placed boundaries in. We placed the rectangular elements like obstacles on both sides of the channel. On the bottom and also on the top of the channel, to have them symmetrical. These obstacles represent roughness in our channel walls. In the Figure 7.3 you can see our definition of roughness on the bottom wall.
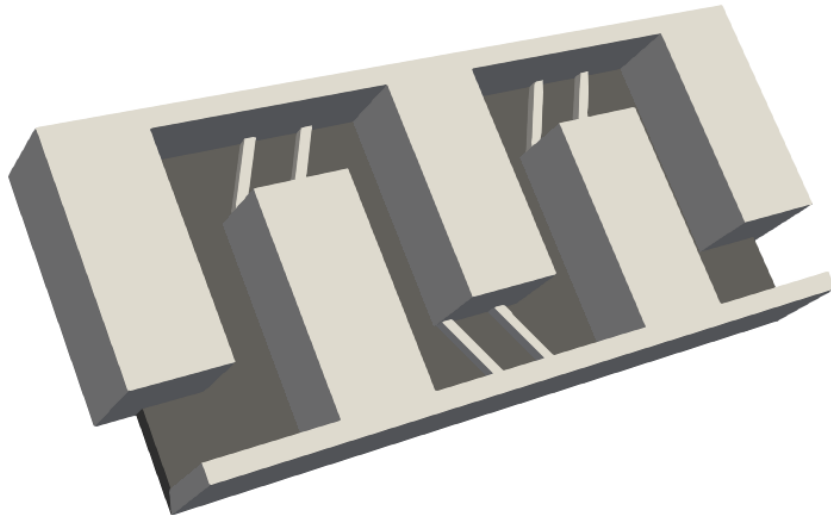
Figure 7.3: Simulation box in 3D with roughness (thin rhomboids with light grey colour) on bottom wall for the case of the cross-section with dimensions $60 \times 52 \mu m$.

In the Figure 7.4 we can see the fluid flow in the channel with roughed walls. The roughness elements were added to the channel as obstacles, created in ESPResSo via rhomboids. The height of roughness elements is set up to 10 μm, the distance between the elements is set up to 40 μm, size of roughness is set up to 10 μm for both roughness elements at the top and at the bottom of the channel. The rhomboids are added to three places in the simulation box across the whole channel width, in this case across the whole 60 μm.
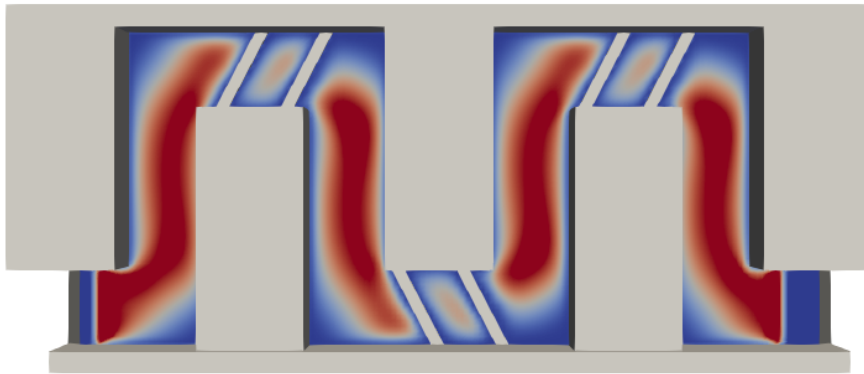
Figure 7.4: Simulation box in 2D for the case of the cross-section with dimensions $60 \times 52 \mu m$ with roughness and with fluid flow with flow velocity of 0.6 $\mu m / \mu s$. Red colour represents maximal flow velocity.

In the Figure 7.5 you can see the places in simulation box for visualisation cuts, where we analysed the Dean effect in channels with roughned walls. Some of the roughness elements extend to the visualisation cuts.
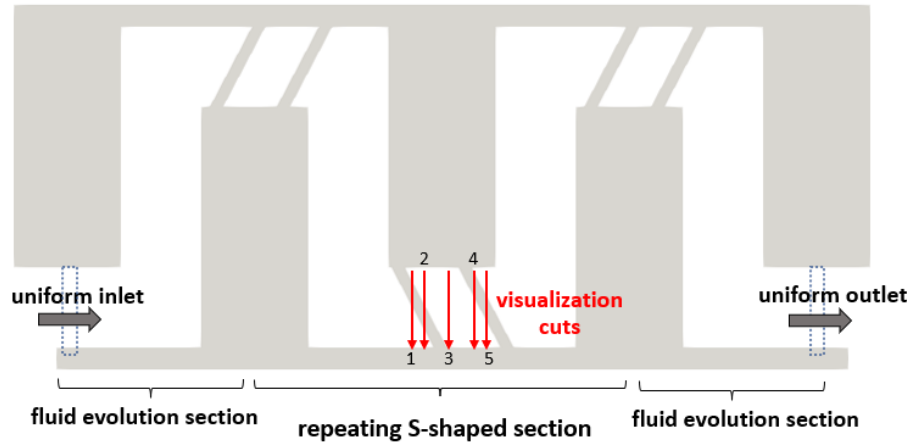
Figure 7.5: Simulation box in 2D for the case of the cross-section with dimensions $60 \times 52\mu m$ with roughness. Visualisation cuts 1,2,3,4 and 5 for Dean's effect is depicted with red colour.

7.3   Results

Our interest in this chapter was to define roughness to our square serpentine channel with dimensions $60 \times 52\mu m$. We had more possibilities how to define it and we chose roughness elements to the top and bottom of the channel.

Secondly, we need to find out how the Dean vortices in the cross-section change when we compare channel without roughness and with roughness. We did this comparison without particles immersed at the beginning. Flow velocity in the simulations was set up to 0.6 $\mu m/\mu s$.

Let's see the Dean effect in our square serpentine channel geometry without roughness first, Figure 7.6. In the middle of the simulation box with dimensions $60 \times 52\mu m$ we have a visualisation cut. When we do a cross-section of the channel and remove the main axial direction, we can see secondary flow existing in parallel to the y-axis. It is composed of two symmetrical streamlines - Dean vortices. It is caused by Dean drug force and the streamlines copy the channel cross-section. Dean vortices are situated almost in the middle of the channel. The coloring is according the speed of this secondary flow.
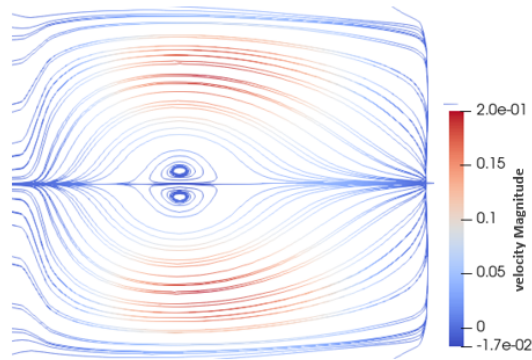
Figure 7.6: Dean vortices in the channel cross-section with dimensions $60 \times 52 \mu m$ without any roughness. Flow velocity in the simulation was set up to 0.6 $\mu m/\mu s$. Visualisation from visualisation cut 3.

In Figure 7.7 we can see Dean forces streamlines in cross-section for the channel with dimensions $60 \times 52 \mu m$ with rectangular elements in the walls, defined as a roughness. The visualisation cut used for this figure was in the middle of the simulation box. Dean vortices are symmetrical and situated near the outer wall. They copy the form of the channel cross-section. On the right side we can see two similar places with almost no streamlines. This is caused by two roughness elements which were added to the channel as the obstacles. The coloring is according the speed of this secondary flow.
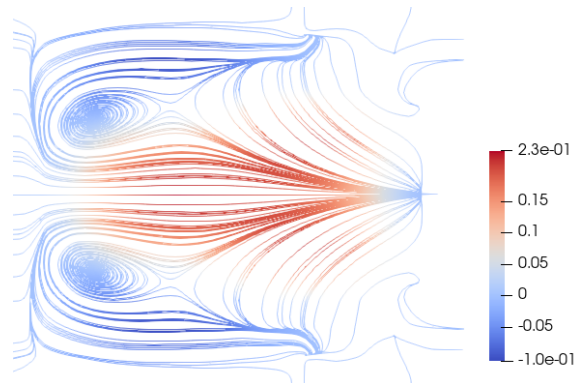
Figure 7.7: Dean vortices in the channel cross-section with dimensions $60 \times 52 \mu m$ with rectangular roughness. Flow velocity in the simulation was set up to 0.6 $\mu m/\mu s$. Visualisation from visualisation cut 3.

In five visualisation cuts in Figure 7.8, we can see Dean vortices in cross-section, without particles immersed. Simulation run with fluid velocity of $0.45\mu m/\mu s$. It can be seen, some of the roughness elements extend to the visualisation cuts and thus to the Dean vortices. We see it like places with almost no streamlines in visualisation cut 1 and in visualisation cut 5. They are placed in the middle of the cross-section on the channel top and on the channel bottom. In visualisation cut 2, this places are shifted little bit to the outer wall and in visualisation cut 4 to the inner wall. In visualisation cut 3 we do not see this places, while these roughness elements do not extend to the cross-section.

cross-section 60x52µm; velocity fluid 0.45 µm/µs
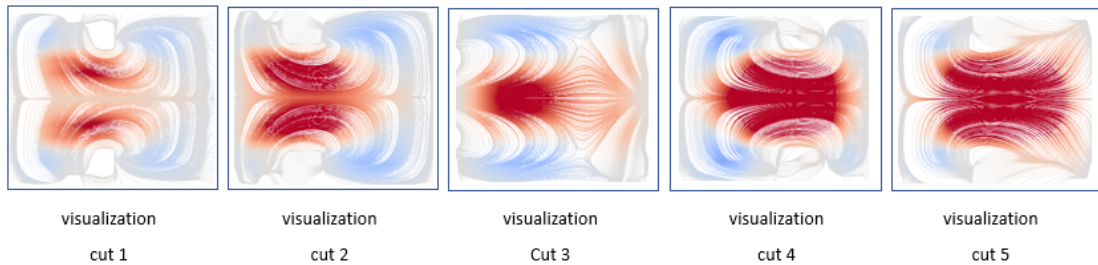
Figure 7.8: Visualisation cuts from the goemetry of 60x52 cross-section.

Our hypothesis is, that this roughness elements will influence the simulations with particles immersed to the flow. For the verification, more analyses is needed.

7.4 Discussion

For an instructive analyses of the impact of roughned channel walls to the particular separation performance we need to simulate many cases with different settings. We can change roughness elements, their shape, size and high, the distance between them, their position across the channel width and also position across the whole simulation box or their slope under which we insert them into the channel walls. In this Chapter we started with rectangular roughness elements in the top and bottom of the channel and we have some picture and ideas about the problem. But still we are at the beginning in this theme and further simulations and analyses are needed.

During our first analyses of first draft of roughness in microchannel without particles, we realized that the roughness elements affect the Dean drug force and thus Dean vertices observed in channel cross-section. In contrast to ordinary square serpentine microchannel without roughness, vertices are pushed to the wall, because the roughness elements narrow the direction of the channel. This behavior can be inferred since we added the elements as obstacles.

The topic of rough channels is very broad/wide. To conclude, this simulation study demonstrates, it is important to consider the position of roughness elements and why the further analyses are crucial.

We therefore suggest:

- study further and find some other sources regarding roughness

- consider other roughness elements - analyse different distance between the elements, consider different elements high and elements size

- analyse further channel geometries possibilities

- other roughness definition completely

- particle seeding to the channel with roughness to see the impact on particle focusing performance

8 Summary

In our doctoral work, we dealt with inertial flow in curved channels, identification of Dean vortices in several geometries and we present several scenarios how to separate particles depending on their size and how the roughness of the channel walls affects these results.

First, we began with a study of literature and articles about inertial flows and their properties in curved channels, which are influenced by several parameters, especially the Dean number. We studied and compared several geometries analyzed in existing research of microfluidic devices. Our biological motivation was described in Chapter 1. After studying we focused more on our goal, which was defined at the beginning of doctoral studies and we defined partial objectives leading to this goal. Chapter is finished with thesis outline.

In Chapter 2 we started with sum up of ongoing situation in particle separation with different sizes in different geometries of channels. We focused there to specify basic existing model parts for our research needs. We described simulation box, fluid model with two different types of fluid moving and elastic object model which were enabled by the open-source software ESSPResSo and PyOIF software package for this software. Interactions between individual models were also described. The chapter is finished with an overview of supporting hardware.

In Chapter 3 we went over the inertial effects in curved channels. There are some differences between fluid flow in straight and curved channels. We described competing inertial forces responsible for particle separation performance, while the flow is effected by them. Besides wall interaction lift forces and shear gradient lift forces, in curved channels we can observe Dean drag force in addition. The chapter is supplemented by formulas for the evaluation of these forces.

We then started to design a suitable channel geometry to verify the Dean effect and also set suitable parameters for the simulations that we compared with each other in Chapter 4. In order to optimize the simulation time in these devices, a relevant geometry of channels is crucial. We spent a lot of time trying to get the most suitable geometry. By analyzing the results of simulations with different settings, we improved the geometry of the channel. We simulated the fluid flow as a periodical flow thanks to particle reseeding. During the flow moving set up we discussed particle re-seeding artefact, which did us problems with flow periodicity and thus problems with trajectories of particles.

In Chapter 5, Dean effects in the channel cross sections were visualized. We showed three different geometries, namely a cylindrical ring with a squared cross-section, torus with circular cross-section and a helix with a circular cross-section. At the beginning we briefly described an implementation of analyzed geometries in ESPResSo. For these various cross-sections we run several simulations. The simulations differ by parameters in order to see an impact on the fluid flow. We analyzed Dean effect and Dean vortices in cross-sections and the fastest velocity flow without particles. We found that in all three geometries, the maximum fluid flow velocity in the curved channel cross-section is dependent on the magnitude of the Dean number. It is true that the higher the Dean number, the closer the maximum fluid flow velocity is to the outer wall of the curved channel. The main conclusion is about fastest flow depended also on other parameters like curvature radius, section radius and kinematic viscosity. In addition, we noticed that the geometry of the channel itself causes differences in the results, as can be seen in the graphs. In all three case geometries, these Dean vortices are defined by the given geometry, thus proving the presence of a secondary flow in the fluid flow, which causes the Dean effect.

In Chapter 6 we designed a suitable microchannel for particle separation. From typical shapes of channels used in inertial microfluidics we chose square serpentine channel for our study. We compared particles of two sizes: $5\mu m$ and $10\mu m$ with four average fluid flow velocities: 0.18, 0.35, 0.45 and finally 0.6 $\mu m/\mu s$. Further we compared three types of cross-sections in channel geometries: 60×52 μm, 80×40 μm and 100×32 μm. We realised, that the channel type of 80×40 μm has the best particle focusing performance and the geometry is suitable for particle separation

based on their size. Higher throughput is possible due to large Reynolds number and thus larger fluid velocity. We are happy to see our results similarity with existing researches in the world. Based on this, we can tell our research is verified.

At the end, in last Chapter 7 we tested roughness elements defined on the top and bottom of the channel walls. Despite the roughness is primarily used in different way in simulations, to simulate imperfect channel walls, because during the manufacturing 100 % smooth channel walls are not possible and real, we defined roughness differently by obstacles in channel walls. In this final part of our research, we present preliminary computational results showing the effect of the roughness on the channel walls on fluid flow inside the channels. Further investigation would include particles to show the impact on sorting performance.

We supplemented the individual parts with pictures, tables, schematic pictures and pictures from simulations.

8.1 Contribution of this thesis

To sum up, the main contribution of the thesis to applied computer science and computational modeling in microfluidics are:

- Providing detailed analysis of the Dean effect in various channel geometries

- Using computational model for design optimization of microfluidic channels with respect to particle sorting

- Design of roughness on the channel walls of the selected channel and comparison of results with the channel without roughening

All published results, achieved within this thesis, are listed in Section 8.3.

8.2   Future goals and closing remarks

Microfluidic devices represent a unique powerful tool for working with living cells. These miniaturized systems allow detailed analyzes to be performed with many advantages. Lab-on-chip microfluidic technologies are revolutionizing laboratory experiments and bringing the benefits of miniaturization to the research around the world. As the real construction of their prototypes is technologically demanding and also costs a lot of money, simulations before constructions of these microchips are important.

Small sized microfluidic chips have potential to separate cells according to their size and/or density. In terms of detection the right microchannel, for the future use of the described approaches, further simulations is imperative for any progress. It is however of note, that further improvements are not trivial not only from the research and studying, but also from the time-consuming. This is the reason why the right geometry of the channel is so crucial. Inertial focusing in channels is highly sensitive to geometry of the channel and dynamical properties of the fluid. The transversal position of cells is affected either by the lift forces (induced by the shear flow or by the channel wall) or by secondary flows called the Dean flows. The complexity of the problem is enormous.

Roughness in microchips represents also a goal for the future. In our work we started with some proposals, but still we need to analyse it more. We need to find out the best design for roughness placement into the microchannel. A lot of studying and a lot of analyses is still needed here.

CTCs are the main reason for cancer metastizing. Formation of clusters of CTCs increase their metastatic potential. The next study of CTC clusters is crucial in understanding of their role in disease development and treatment. Scarcity of CTCs in blood requires high-throughput systems for their isolation. In terms of next steps, we need to analyze cell clusters. We would like to employ blood cell models to create computational models of cell clusters. The models will be validated on microfluidic experiments. The experiments will measure the hydrodynamics of cell sorting and adhesion strength of individual cells in a cluster.

The current call of Global Seeds Slovakia gave a great opportunity to start a new collaboration between the two groups for an exciting joint project. The MIT (Massachusetts Institute of Technology) group specializes in microfluidic assays for testing cell deformability as well as sorting circulating tumor cells and cell clusters. In cooperation with colleagues from MIT, we are interested in creating real microchannels and in microchannels with a roughened surface and verifying some properties of the fluid flow in them. We will employ the "modelling meets experiments" approach when both modelling and experiments complement each other: experiments give real data for e.g. model validation and computational model gives results for rapid prototyping the new devices.

After validation of our existing models, there is still a lot of potential in finding new ways of how to construct the right channel in simulations in terms of computer and software support. There are some possibilities how to fix the problems with fluid movement in the channel in the ESPResSo package.

Overall, this area of the improvement of microfluidic devices simulations shows a lot of promises going into the future as well as study of particles and fluid flow.

8.3 Published papers

[1] Bohiniková, A., Maia, I., Smiešková, M., Bugáňová, A., Moita, A.S., Cimrák, I. and Lima, R.A.: *Assessment of Computational Cell Model Benefits for Optimization of Microfluidic Devices*, In Proceedings of the 13th International Joint Conference on Biomedical Engineering Systems and Technologies, Vol.1, (2020), p. 280-287, Science and technology publications, SciTePress, INSTICC, doi: 10.5220/0009173202800287, ISBN: 978-989-758-398-8, ISSN: 2184-4305

[2] A. Bugáňová, *Special geometry of the microchannel for the verification of Dean's flow hypothesis*, In Mathematics in science and technologies, MIST conference 2020

[3] I. Cimrák and A. Bugáňová, *PYOIF in Espresso: A 3D Computational Tool for Modelling Flow of Multicell Systems*, In Journal of Information, Control and Management Systems, Vol.17, (2019), No.2

[4] A. Bugáňová, *Dean's vortex and a special geometry of the channel* In: Fluid flow and Microfluidics, 3rd Workshop on Modelling of Biological Cells, (2020)

[5] Bugáňová, A., Cimrák I. and Kovalčíková, K.: *Computational Study of Inertial Effects in Toroidal and Helical microchannels*, Computational Systems-Biology and Bioinformatics, (2020), Association for Computing Machinery, New York, NY, USA, Pages 3–10, https://doi.org/10.1145/3429210.3429222

[6] Bugáňová, A., Cimrák, I. and Kovalčíková, K.: *Modelling of Arbitrary Shaped Channels and Obstacles by Distance Function*, Bioinformatics and Biomedical Engineering, (2022), Springer International Publishing, pages 28-41, ISBN: 978-3-031-07704-3, doi: 10.1007/978-3-031-07704-3-3

[7] Bugáňová, A. and Cimrák, I.: *Computational study of particle separation based on inertial effects in rectangular serpentine channels with different aspect ratios*, Proceedings of the 16th International Joint Conference on Biomedical Engineering Systems and Technologies (BIOSTEC 2023) - BIOINFORMATICS, (2023), pages 284 - 291, SciTePress, INSTICC, ISBN: 978-989-758-631-6, doi: 10.5220/0011788200003414

Bibliography

[1] Arnold, A., Lenz, O., et al.: 'ESPResSo 3.1: Molecular dynamics software for coarse-grained models', *Meshfree Methods for Partial Differential Equations VI*, vol. 89 of *Lecture notes in computational science and engineering*, pp. 1–23, Springer Berlin Heidelberg, Berlin, Heidelberg, 2013, ISBN 978-3-642-32978-4, doi:10.1007/978-3-642-32979-1_1

[2] Bachraty, H., Bachratá, K., et al.: *Simulation of Blood Flow in Microfluidic Devices for Analysing of Video from Real Experiments*, pp. 279–289, Lecture notes in computer science, Springer International Publishing, Cham, 2018, ISBN 978-3-319-78722-0, doi:10.1007/978-3-319-78723-7_24

[3] Bugáňová, A., Cimrák, I.: 'Computational study of particle separation based on inertial effects in rectangular serpentine channels with different aspect ratios', Springer International Publishing, in publication process, 2023

[4] Cell-in-fluid research group: 'Cell-in-fluid research group', doi:https://cellinfluid.fri.uniza.sk

[5] Cell-in-fluid research group: 'esspresso', doi:https://github.com/icimrak/espresso/tree/python

[6] Chun, B., Ladd, A.J.C.: 'Inertial migration of neutrally buoyant particles in a square duct: An investigation of multiple equilibrium positions', *Physics of Fluids*, vol. 18, no. 3, 2006, ISSN 1070-6631, doi:10.1063/1.2176587, 031704

[7] Cimrák, I., Gusenbauer, M., Jančigová, I.: 'An ESPResSo implementation of elastic objects immersed in a fluid', *Computer Physics Communications*, vol. 185, no. 3, pp. 900 – 907, 2014, ISSN 0010-4655, doi:http://dx.doi.org/10.1016/j.cpc.2013.12.013

BIBLIOGRAPHY

[8] Di Carlo, D., Edd, J.F., et al.: 'Particle segregation and dynamics in confined flows', *Phys. Rev. Lett.*, vol. 102, p. 094503, 2009, doi:10.1103/PhysRevLett.102.094503

[9] Dinler, A., Okumus, I.: 'Inertial particle separation in curved networks numerical study', *Chemical Engineering Science*, pp. 119–131, 2018

[10] Eckhart, R., Redlinger-Pohn, J., et al.: 'The effect of dean flow in a tube flow fractionation device', *Nordic Pulp and Paper Research Journal*, vol. 31, no. 4, pp. 641–647, 2016

[11] Fakhrodin Lalegani, Mohammad Reza Saffarian, A.M., Tavousi, E.: 'Effects of different roughness elements on friction and pressure drop of laminar flow in microchannel', *International Journal of Numerical Methods for Heat and Fluid Flow*, vol. 391, p. 123570, 2018, doi:10.1108/HFF-04-2017-0140

[12] Gossett, D.R., Tse, H.T.K., et al.: 'Hydrodynamic stretching of single cells for large population mechanical phenotyping', *Proc. Natl. Acad. Sci. U. S. A.*, vol. 109, no. 20, pp. 7630–7635, 2012

[13] Gou, Y., Jia, Y., et al.: 'Progress of inertial microfluidics in principle and application', *Sensors*, vol. 18, no. 6, p. 1762, 2018, doi:https://doi.org/10.3390/s18061762

[14] Hood, K., Lee, S., Roper, M.: 'Inertial migration of a rigid sphere in three-dimensional poiseuille flow', *Journal of Fluid Mechanics*, vol. 765, pp. 452–479, 2015, doi:10.1017/jfm.2014.739

[15] Jančigová, I.: 'Computational modeling of blood flow with rare cell in a microbifurcation', G.A. Ateshian, K.M. Myers, J.M.R.S. Tavares, eds., *Lecture Notes in Computational Vision and Biomechanics*, Lecture notes in computational vision and biomechanics, pp. 518–525, Springer International Publishing, Cham, 2020, doi:10.1007/978-3-030-43195-2_42

[16] Jančigová, I., Kovalčíková, K., et al.: 'Spring-network model of red blood cell: From membrane mechanics to validation', *Int. J. Numer. Methods Fluids*, vol. 92, no. 10, pp. 1368–1393, 2020

[17] Jančigová, I., Kovalčíková, K., et al.: 'Pyoif: Computational tool for modelling of multi-cell flows in complex geometries', *PLOS Computational Biology*, vol. 16, pp. 1–21, 2020

[18] Jančigová, I., Kovalčíková, K., et al.: 'Pyoif: Computational tool for modelling of multi-cell flows in complex geometries', *PLOS Computational Biology*, vol. 16, no. 10, pp. 1–21, 2020, doi:10.1371/journal.pcbi.1008249

[19] Jančigová, I., Tóthová, R.: 'Scalability of forces in mesh-based models of elastic objects', *2014 ELEKTRO*, pp. 562–566, IEEE, 2014, doi:10.1109/ELEKTRO.2014.6848960

[20] Kosa, B., Mikula, K.: 'Direct simple computation of middle surface between 3d point clouds and/or discrete surfaces by tracking sources in distance function calculation algorithms', 2021

[21] Kovalčíková, K., Bugáňová, A., Cimrák, I.: 'Computational study of inertial effects in toroidal and helical microchannels', CSBio2020, p. 3–10, Association for Computing Machinery, New York, NY, USA, 2020, ISBN 9781450388238, doi:10.1145/3429210.3429222

[22] Kovalčíková Ďuračíková, K., Bugáňová, A., Cimrák, I.: 'Modelling of arbitrary shaped channels and obstacles by distance function', p. 28–41, Springer-Verlag, Berlin, Heidelberg, 2022, ISBN 978-3-031-07703-6, doi:10.1007/978-3-031-07704-3_3

[23] Lu, H., Xu, M., et al.: 'Effects of surface roughness in microchannel with passive heat transfer enhancement structures', *International Journal of Heat and Mass Transfer*, vol. 148, p. 119070, 2020, ISSN 0017-9310, doi:https://doi.org/10.1016/j.ijheatmasstransfer.2019.119070

[24] Matas, J.P., Morris, J., GUAZZELLI, E.: 'Lateral force on a rigid sphere in large-inertia laminar pipe flow', *Journal of Fluid Mechanics*, vol. 621, pp. 59 – 67, 2009, doi:10.1017/S0022112008004977

[25] McLaughlin, J.B.: 'The lift on a small sphere in wall-bounded linear shear flows', *Journal of Fluid Mechanics*, vol. 246, no. -1, pp. 249–265, 1993, doi:10.1017/S0022112093000114

[26] Ookawara, S., Higashi, R., et al.: 'Feasibility study on concentration of slurry and classification of contained particles by microchannel', *Chemical Engineering Journal*, vol. 101, no. 1, pp. 171–178, 2004, ISSN 1385-8947, doi:https://doi.org/10.1016/j.cej.2003.11.008, 7th International Conference on Microreaction Technology

[27] Paraview: 'Paraview', doi:https://www.paraview.org/

[28] Peng, Y., Zarringhalam, M., et al.: 'Effects of surface roughness with the spherical shape on the fluid flow of argon atoms flowing into the microchannel, under boiling condition using molecular dynamic simulation', *Journal of Molecular Liquids*, vol. 297, p. 111650, 2020, ISSN 0167-7322, doi:https://doi.org/10.1016/j.molliq.2019.111650

[29] Tanaka, T., Ishikawa, T., et al.: 'Separation of cancer cells from a red blood cell suspension using inertial force', *Lab Chip*, vol. 12, no. 21, pp. 4336–4343, 2012

[30] Tang, H., Niu, J., et al.: 'Geometric structure design of passive label-free microfluidic systems for biological micro-object separation', *Microsystems and Nanoengineering*, vol. 8, 2022, doi:10.1038/s41378-022-00386-y

[31] Tang, L., Tang, Y., Parameswaran, S.: 'A numerical study of flow characteristics in a helical pipe', *Advances in Mechanical Engineering*, vol. 8, no. 7, p. 1687814016660242, 2016, doi:10.1177/1687814016660242

[32] Tothova, R., Jancigova, I., Busik, M.: 'Calibration of elastic coefficients for spring-network model of red blood cell', *2015 International Conference on Information and Digital Technologies*, pp. 376–380, IEEE, 2015

[33] Vtk: 'vtk', 2020, doi:http://www.vtk.org/

[34] Ward, K., Hugh Fan, Z.: 'Mixing in microfluidic devices and enhancement methods', *Journal of Micromechanics and Microengineering*, vol. 25, no. 9, 2015

[35] Warkiani, M.E., Guan, G., et al.: 'Slanted spiral microfluidics for the ultra-fast, label-free isolation of circulating tumor cells', *Lab Chip*, vol. 14, pp. 128–137, 2014, doi:10.1039/C3LC50617G

[36] Ye, T., Phan-Thien, N., et al.: 'Red blood cell motion and deformation in a curved microvessel', *Journal of Biomechanics*, vol. 65, pp. 12–22, 2017, ISSN 0021-9290, doi:https://doi.org/10.1016/j.jbiomech.2017.09.027

[37] Ying, Y., Lina, Y.: 'Inertial focusing and separation of particles in similar curved channels', *Scientific reports, natureresearch*, vol. 391, p. 123570, 2020, doi:https://doi.org/10.1016/j.cej.2019.123570

[38] Zhang, J., Yan, S., et al.: 'High throughput extraction of plasma using a secondary flow-aided inertial microfluidic device', *RSC Adv.*, vol. 4, pp. 33149–33159, 2014, doi:10.1039/C4RA06513A

[39] Zhang, J., Yan, S., et al.: 'Fundamentals and applications of inertial microfluidics: A review', *Lab Chip*, vol. 16, 2015, doi:10.1039/C5LC01159K